Contemporary Mathematics
https://ojs.wiserpub.com/index.php/CM/

Research Article

On the Interplay of Micropolarity and Viscoelastic Relaxation in Controlling Drag Within a Cavity Flow

Khizar Hayat Khan[1], Muhammad Sabeel Khan[2], Nazim Hussain Hajano[3], Farxod Akmalovich Ixtiyarov[4], Saeed Islam[5*], Amna[6], Ghulam Khadija[2], Muhammad Bilal[2]

[1]Department of Mathematics, College of Science and Humanities, Prince Sattam Bin Abdulaziz University, Al-Kharj, Saudi Arabia
[2]Department of Mathematics, Capital University of Science and Technology, Islamabad, Pakistan
[3]Department of Mathematics, Sukkur IBA University, Sukkur, Pakistan
[4]Center of Research and Innovation, Asia International University, Bukhara, Uzbekistan
[5]Department of Mechanical Engineering, Prince Mohammad Bin Fahd University, Al Khobar, Saudi Arabia
[6]Department of Mathematics, Women University, Swabi, KP, Pakistan
E-mail: SISLAM@pmu.edu.sa

Received: 25 December 2025; **Revised:** 2 February 2026; **Accepted:** 6 February 2026

Abstract: The interplay between microrotation, microinertia, and viscoelastic relaxation significantly influences the hydrodynamic performance of non-Newtonian cavity flows. This study investigates the combined effects of the Eringen number, micropolar coupling constant, and fluid relaxation factor on drag force, microrotation, and flow behavior in a two-dimensional lid-driven cavity. The governing nonlinear partial differential equations are formulated using Eringen's micropolar theory with relaxation-time-dependent stress, and the characteristic Galerkin finite element method is employed for numerical solution using a custom FreeFEM++ implementation. The results reveal a strong coupling between microrotation and viscoelastic relaxation effects. Increasing the relaxation factor enhances flow elasticity, leading to variations in drag force depending on the flow regime. The Eringen number stabilizes the flow and suppresses drag oscillations, while the micropolar coupling constant modulates shear-layer thickness and vortex intensity. Higher Eringen number increases kinetic energy and produces more ordered streamline patterns, whereas larger values of micropolar constant reduces drag while amplifying microrotation. Overall, tuning Eringen number, micropolar constant and time relaxation provides an effective mechanism for controlling drag and optimizing flow stability. These findings offer valuable insights for the design of advanced microfluidic and rheological systems where microstructural and viscoelastic effects coexist.

Keywords: micropolar fluid, Eringen number, relaxation factor, drag force, finite element method, FreeFEM++, lid-driven cavity flow, sustainable engineering design, energy-efficient flow control, industry and innovation

MSC: 65L05, 34K06, 34K28

Nomenclature

u	Velocity components in x-directions
v	Velocity components in y-directions

Copyright ©2026 Saeed Islam, et al.
DOI: https://doi.org/10.37256/cm.7220269430
This is an open-access article distributed under a CC BY license
(Creative Commons Attribution 4.0 International License)
https://creativecommons.org/licenses/by/4.0/

w	Microrotation (angular velocity of microelements)
p	Pressure field
Ψ	Stream function
Fd	Drag force
Re	Reynolds number ($Re = \rho UL/\mu$)
Er	Eringen number (micropolar coupling parameter)
Rf	Fluid relaxation factor (time relaxation parameter)
K	Micropolar constant (vortex viscosity parameter)
ρ	Fluid density
μ	Dynamic viscosity
γ	Spin-gradient viscosity
j	Microinertia density
L	Characteristic length scale (cavity dimension)
U	Lid velocity (driving velocity at the top boundary)
KE	Kinetic energy of the flow
Ω	Computational domain

1. Introduction

Numerous significant events are surrounded by complicated fluids in nature, such as viscoelastic or microfluidic mixtures; as a result, research into these fluids is crucial to the advancement of many industrial operations. These industrial operations include the melting of polymers [1], the production of pulp fibers [2], the processing of minerals [3], the processing of food [4], the production of cement pastes and cosmetics [5], and biophysical processes [6]. It has also been observed that the vibration of nanostructures and the references they contain can induce viscoelastic flows in simple liquids.

So far, the literature has explored viscoelastic flow behavior in various contexts. For instance, in his PhD dissertation [7], Qin investigated the flow of a polymeric viscoelastic fluid across three different geometries and discovered that fluid relaxation influences the onset of turbulence in shear flows. Yuan et al. [8] presented a comprehensive review on the impact of viscoelastic fluid flows and their applications. Zhu et al. [9] examined the swimming of ciliated cells in a viscoelastic Giesekus fluid and reported a decrease in flow velocity in the presence of polymeric stresses, focusing particularly on the influence of the Weissenberg number. Viscoelastic microfluidics are also widely used to simulate blood flow in the human body with important health applications, as discussed in the review by Sebastian and Dittrich [10]. Haward et al. [11] studied viscoelastic fluids in porous media, and Liu et al. [12] investigated Bacillus population separation in microfluidics using viscoelastic fluids. Alves et al. [13] provided an extensive review of numerical approaches for viscoelastic fluid flows.

Despite the above efforts, the impact of fluid relaxation time in these models has been rarely examined in depth, even though it has significant implications. A few works study relaxation time in specific situations. Mahapatra and Bandopadhyaya [14] examined the impact of fluid relaxation and retardation time in electro-osmosis of viscoelastic fluids over a non-uniformly charged surface. Dey [15] studied hydromagnetic viscoelastic flow in annular regions and found that relaxation time strongly influences maximum velocity near the center of the domain. Eldesoky [16] considered compressible Maxwellian peristaltic slip flow and analyzed the role of relaxation time in one-dimensional models. These studies show the importance of fluid memory, but comprehensive numerical investigations of relaxation time in confined cavity flows remain scarce. In recognition of its numerous commercial and technological uses, the study of conducting micropolar fluids has also grown in importance. Micropolar fluids, introduced by the Cosserat brothers [17] and formulated in detail by Eringen [18], are a subclass of non-Newtonian fluids whose microelements possess independent microrotation. Their anisotropic nature makes them appropriate for modeling complex fluids such as liquid crystals, polymeric suspensions, colloidal solutions, blood, paints, and lubricants [19]. Micropolar theory introduces new parameters such as spin gradient viscosity, vortex viscosity, and most importantly the micro-inertia parameter, which leads

to the nondimensional Eringen number. Sharma et al. [20] demonstrated applications of micropolar fluids in lubrication to reduce skin friction. Khan [21] and Karvelas et al. [22] have shown micropolar models provide more comprehensive explanations for blood flow in arteries and microchannels compared to classical fluids. Magnetization combined with micropolar theory has been explored by Eringen [23], who studied electrodynamics and Magnetohydrodynamics (MHD) of micropolar fluids. Saraswathy et al. [24] examined nonlinear thermal radiation and viscous dissipation in MHD micropolar fluids through porous channels, reporting reversal phenomena in microrotation profiles. Almakki [25] introduced a micropolar nanofluid model with entropy generation using a stretched boundary layer. Yasmeen et al. [26] investigated micropolar and non-Newtonian nanofluid flows incorporating the Cattaneo-Christov heat flux model, highlighting the influence of microrotation and thermal relaxation. In a related study, Yasmeen et al. [27] examined Carreau-type nanofluid flow and reported that relaxation heat flux and slip mechanisms significantly affect the velocity and temperature fields. Eldabe et al. [28] explored peristaltic transport in complex geometries and demonstrated that thermal relaxation, Hall effects, and coupled heat-mass transfer play important roles in governing flow behavior and microrotation. Abd El Aziz [29] analyzed stagnation point MHD nanoflows with magnetic induction. Narayana [30] studied hall current and radiation absorption in rotating micropolar flows. Goud [31] examined heat generation and absorption in micropolar MHD flows through porous surfaces. Khan et al. [32] applied the finite element method to MHD micropolar flows in rectangular channels, showing that magnetic induction and microrotation decrease with stronger micropolar coupling. These studies highlight the flexibility of micropolar fluids in modeling real-world engineering and biomedical problems. However, none of these works has explicitly analyzed the coupled effect of micro-inertia (captured by the Eringen number) and relaxation time on drag force in confined cavity flows. The lid-driven cavity problem is a classical benchmark for testing numerical methods and understanding fundamental shear-driven fluid dynamics. It involves a square cavity driven by the motion of the top lid at constant velocity, while the remaining walls remain stationary. The geometry produces primary and secondary vortices that are sensitive to physical parameters. For Newtonian fluids, cavity flow has been extensively investigated. However, for micropolar-viscoelastic fluids, the combined role of Eringen number and relaxation factor remains underexplored. Most studies treat either micropolar effects or viscoelastic relaxation in isolation, leaving a clear research gap.

The present study addresses this gap by conducting a systematic numerical investigation of the effect of Eringen number and relaxation factor on drag force in a lid-driven cavity. The governing equations of micropolar-viscoelastic fluids are formulated in nondimensional form using Reynolds number, relaxation factor, and Eringen number as control parameters. The finite element variational framework is implemented in FreeFEM++ [33], enabling robust simulation of the coupled velocity and microrotation fields. The numerical experiments quantify how micro-inertia and fluid memory interact to alter drag distributions and flow topology. Results reveal that Eringen number can either enhance or mitigate the influence of relaxation on drag, depending on the flow regime. Despite extensive research on micropolar and viscoelastic fluid flows, the combined influence of micro-inertia (captured by the Eringen number) and viscoelastic relaxation time on drag in confined cavity flows remains largely unexplored. Understanding this interplay is crucial for practical applications where precise control of flow resistance and vortex structures is required, such as in microfluidic devices, lubrication systems, polymer processing, and biomedical flows. The novelty of the present study lies in systematically isolating and quantifying the effects of Eringen number, micropolar coupling, and relaxation factor on cavity drag and flow stability, using a robust Finite Element Method (FEM) framework implemented in FreeFEM++. By bridging the gap between micropolar microstructural dynamics and viscoelastic fluid memory, this work provides new insights for designing and optimizing confined non-Newtonian flows beyond classical Newtonian assumptions.

The remainder of this paper is organized as follows. Section 2 presents the problem description and the mathematical formulation of the viscoelastic micropolar flow within a cavity, followed by the constitutive modeling of the micropolar viscoelastic fluid and the governing equations in vector form. The non-dimensionalization procedure is then discussed to introduce key dimensionless parameters governing the system behavior. The weak formulation and numerical algorithm implemented in the FreeFEM++ framework are detailed subsequently. Section 3 provides a comprehensive discussion of the numerical results, including a validation of the proposed model. Finally, Section 4 summarizes the main findings and highlights the physical implications of the combined effects of the Eringen number, micropolar constant, and relaxation factor on the drag characteristics of cavity flow.

2. Problem description and mathematical modeling

We consider an unsteady, two-dimensional, incompressible viscoelastic micropolar fluid confined within a square lid-driven cavity as depicted in Figure 1. The top boundary of the cavity moves at a constant horizontal velocity u_0, while all other boundaries are stationary. The cavity may contain baffles or internal obstructions, which promote complex recirculation zones and enhance the study of drag forces. This configuration is widely used as a benchmark in computational fluid dynamics due to its simple geometry yet rich vortex dynamics.

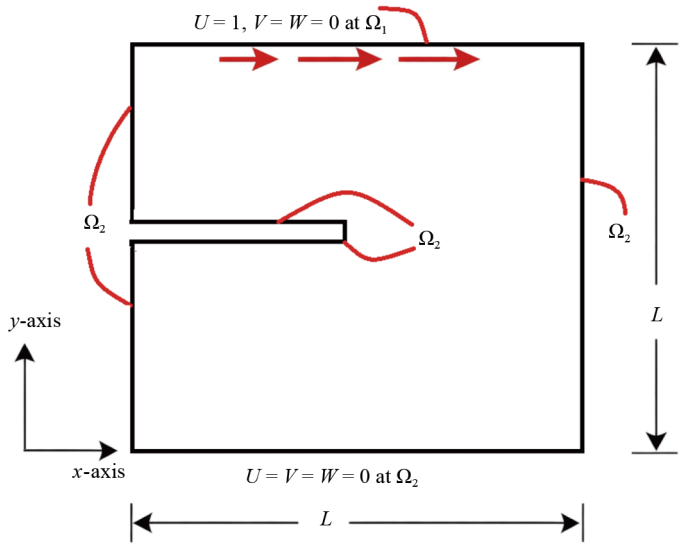


Figure 1. Schematic representation of the lid-driven cavity geometry

Lid-driven cavity flow is a classical benchmark problem in fluid dynamics because it combines simple geometry with complex vortex structures and shear-layer interactions. It is widely used to validate numerical methods and constitutive models, especially for non-Newtonian and microstructured fluids. Cavity type flows also appear in many practical applications, including lubrication and coating systems, polymer and food processing, microfluidic devices, biomedical flows in confined chambers, and cooling of electronic components. Understanding drag and vortex behavior in such confined flows is therefore important for improving mixing, reducing energy losses, and enhancing flow stability in engineering systems.

2.1 *Constitutive modeling of the viscoelastic micropolar fluid*

The constitutive behavior of the fluid is modeled using the Upper-Convected Maxwell (UCM) relation, which accounts for viscoelastic relaxation effects [34]. The extra stress tensor τ satisfies

$$\lambda \nabla_{\tau} + \tau = -2\eta\, \mathbf{d}(\mathbf{v}), \tag{1}$$

where in Eq. (1), λ denotes the fluid relaxation time, η the dynamic viscosity, and $\mathbf{d}(\mathbf{v})$ the rate-of-strain tensor, given by

$$\mathbf{d}(\mathbf{v}) = \frac{1}{2}\left(\nabla \mathbf{v} + (\nabla \mathbf{v})^{T}\right). \tag{2}$$

In Eq. (2), ∇_τ denotes the upper-convected derivative of the stress tensor, defined as

$$\nabla_\tau = \frac{\partial \tau}{\partial t} + \mathbf{v}\cdot\nabla\tau - (\nabla\mathbf{v})\cdot\tau - \tau\cdot(\nabla\mathbf{v})^T. \tag{3}$$

The upper-convected derivative in Eq. (3) provides a frame-invariant description of how stress evolves while being transported and deformed by a moving fluid. The last three terms provide the geometrical correction for deformation of the material frame. They ensure that the derivative is objective, meaning it is independent of rigid-body rotations of the observer. Without these terms, the stress evolution would incorrectly depend on the coordinate system. From a physical viewpoint, the upper convected derivative describes how internal microstructural elements (such as fluid micro-rotations or elastic stresses) are stretched, rotated, and convected with the flow. In viscoelastic fluids, stresses are not only functions of the current deformation but also depend on how fluid elements have been distorted over time. The upper convected derivative therefore captures memory effects, allowing the model to represent elastic behavior in addition to viscous response.

2.2 *Governing equations in vector form*

For incompressible micropolar-viscoelastic fluids without body forces, the conservation laws are expressed in vector form as follows [35]

$$\nabla\cdot\mathbf{v} = 0, \tag{4}$$

$$\rho\left(\frac{\partial \mathbf{v}}{\partial t} + \mathbf{v}\cdot\nabla\mathbf{v}\right) = -\nabla p + \nabla\cdot\tau, \tag{5}$$

$$\rho j\frac{D\boldsymbol{\omega}}{Dt} = \gamma^*\nabla^2\boldsymbol{\omega} + 2k(\nabla\times\mathbf{v} - 2\boldsymbol{\omega}), \tag{6}$$

where, $\mathbf{v} = (u, v)$ is the velocity vector, p is the pressure, τ is the extra stress tensor, $\boldsymbol{\omega}$ denotes the microrotation vector, ρ is the density, j the micro-inertia, γ^* the spin-gradient viscosity, and k the vortex viscosity.

2.3 *Component form of the governing equations*

The component form of the Eqs. (4)-(6) is obtained by expanding in Cartesian coordinates (x, y) as follows.

$$\frac{\partial u}{\partial x} + \frac{\partial v}{\partial y} = 0, \tag{7}$$

$$\frac{\partial u}{\partial t} + u\frac{\partial u}{\partial x} + v\frac{\partial u}{\partial y} + \lambda\left(u^2\frac{\partial^2 u}{\partial x^2} + v^2\frac{\partial^2 u}{\partial y^2} + 2uv\frac{\partial^2 u}{\partial x\partial y}\right)$$

$$= -\frac{1}{\rho}\frac{\partial p}{\partial x} + \frac{1}{\rho}(\mu + k)\left(\frac{\partial^2 u}{\partial x^2} + \frac{\partial^2 u}{\partial y^2}\right) + \frac{k}{\rho}\frac{\partial w}{\partial y}, \tag{8}$$

$$\frac{\partial v}{\partial t}+u\frac{\partial v}{\partial x}+v\frac{\partial v}{\partial y}+\lambda\left(u^2\frac{\partial^2 v}{\partial x^2}+v^2\frac{\partial^2 v}{\partial y^2}+2uv\frac{\partial^2 v}{\partial x\partial y}\right)$$

$$=-\frac{1}{\rho}\frac{\partial p}{\partial y}+\frac{1}{\rho}(\mu+k)\left(\frac{\partial^2 v}{\partial x^2}+\frac{\partial^2 v}{\partial y^2}\right)-\frac{k}{\rho}\frac{\partial w}{\partial x}, \tag{9}$$

$$\frac{\partial w}{\partial t}+u\frac{\partial w}{\partial x}+v\frac{\partial w}{\partial y}=\frac{\gamma^*}{\rho j}\left(\frac{\partial^2 w}{\partial x^2}+\frac{\partial^2 w}{\partial y^2}\right)+\frac{2k}{\rho j}\left(\frac{\partial v}{\partial x}-\frac{\partial u}{\partial y}-2w\right). \tag{10}$$

The Eqs. (7)-(10) constitute the mathematical model for the problem under consideration together with the following boundary conditions.

$$\begin{cases} u=u_0, \quad v=0, \quad w=0, & \text{on the moving lid,} \\ \\ u=0, \quad v=0, \quad w=0, & \text{on the stationary cavity walls.} \end{cases} \tag{11}$$

2.4 *Non-dimensionalization*

To compute the response of the governing flow system in Eqs. (7)-(11), we introduce the following dimensionless variables.

$$U=\frac{u}{u_0}, \quad V=\frac{v}{u_0}, \quad W=\frac{Lw}{u_0}, \quad X=\frac{x}{L}, \quad Y=\frac{y}{L}, \quad T=\frac{u_0 t}{L}, \quad \text{and} \quad P=\frac{p}{\rho u_0^2}, \tag{12}$$

where L is the characteristic cavity length and u_0 is the lid velocity. Using Eq. (12) in Eqs. (7)-(11) the following resulting non-dimensional system is obtained.

$$\frac{\partial U}{\partial X}+\frac{\partial V}{\partial Y}=0, \tag{13}$$

$$\frac{\partial U}{\partial T}+U\frac{\partial U}{\partial X}+V\frac{\partial U}{\partial Y}+A_1\left(U^2\frac{\partial^2 U}{\partial X^2}+V^2\frac{\partial^2 V}{\partial Y^2}+2UV\frac{\partial^2 U}{\partial X\partial Y}\right)=-\frac{\partial P}{\partial X}+A_2\left(\frac{\partial^2 U}{\partial X^2}+\frac{\partial^2 U}{\partial Y^2}\right)+A_3\frac{\partial W}{\partial Y}, \tag{14}$$

$$\frac{\partial V}{\partial T}+U\frac{\partial V}{\partial X}+V\frac{\partial V}{\partial Y}+A_4\left(U^2\frac{\partial^2 V}{\partial X^2}+V^2\frac{\partial^2 V}{\partial Y^2}+2UV\frac{\partial^2 V}{\partial X\partial Y}\right)=-\frac{\partial P}{\partial Y}+A_5\left(\frac{\partial^2 V}{\partial X^2}+\frac{\partial^2 V}{\partial Y^2}\right)-A_6\frac{\partial W}{\partial X}, \tag{15}$$

$$\frac{\partial W}{\partial T}+U\frac{\partial W}{\partial X}+V\frac{\partial W}{\partial Y}=A_7\left(\frac{\partial^2 W}{\partial X^2}+\frac{\partial^2 W}{\partial Y^2}\right)+A_8\left(\frac{\partial V}{\partial X}-\frac{\partial U}{\partial Y}-2W\right). \tag{16}$$

In Eqs. (13)-(16), the values of $A_1, A_2, ..., A_8$ are expressed as

$$A_1 = A_4 = R_f, \quad A_2 = A_5 = \frac{1}{Re}, \quad A_3 = A_6 = \frac{K}{Re}, \quad A_7 = \frac{1}{Re}\left(1 + \frac{K}{2}\right), \quad A_8 = \frac{2K}{E_r Re},$$

where Re is the Reynolds number, R_f is the relaxation factor, K is the micropolar coupling parameter, K_m is the micro-inertial parameter, and E_r denotes the Eringen number and are defined as

$$Re = \frac{\rho L u_0}{\mu}, \quad R_f = \frac{\lambda u_0}{L}, \quad K = \frac{k}{\mu}, \quad K_m = \frac{\gamma^*}{\mu j}, \quad E_r = \frac{j}{L^2}. \tag{17}$$

The boundary conditions in Eq. (11) transforms to

$$\begin{cases} U = 1, \quad V = 0, \quad W = 0, \quad \text{on the moving lid,} \\ \\ U = 0, \quad V = 0, \quad W = 0, \quad \text{on the stationary cavity walls.} \end{cases} \tag{18}$$

The boundary conditions in Eq. (18) are standard for a lid-driven cavity problem and are chosen to allow validation of the present numerical method against classical and micropolar cavity flow results in the literature. On the moving lid, a uniform tangential velocity is imposed in the horizontal direction, with no normal or microrotational motion. This drives the cavity flow and generates vortical structures characteristic of lid-driven cavities. The final system in Eqs. (13)-(18), together with boundary conditions, forms the mathematical model for the viscoelastic micropolar cavity flow under investigation.

2.5 *Weak formulation*

This section presents the variational (weak) formulation of the micropolar cavity flow problem with the inclusion of the Eringen number and relaxation factor, derived from the governing equations (13)-(16). To apply the Finite Element Method (FEM), the physical domain Ω is descretized into a finite number of non-overlapping triangular elements, such that

$$\Omega_h = \bigcup_{i=1}^{n_e} K_i,$$

where K_i denotes the i^{th} triangular element and n_e is the total number of elements in Ω_h. The descretization is obtained so that

$$K_i \cap K_j = \emptyset, \quad \text{for } i \neq j.$$

Let us define the finite element spaces for velocity, pressure, and microrotation fields as

$$\begin{cases} \mathscr{U}_h = \left\{ \mathbf{u} \in \left(H_0^1(\Omega)\right)^2 \;\middle|\; \mathbf{u}|_K \in (P_2)^2,\ \forall K \in \Omega_h \right\}, \\ \mathscr{P}_h = \left\{ p \in L^2(\Omega) \;\middle|\; p|_K \in P_1,\ \forall K \in \Omega_h \right\}, \\ \mathscr{W}_h = \left\{ w \in H_0^1(\Omega) \;\middle|\; w|_K \in P_2,\ \forall K \in \Omega_h \right\}. \end{cases} \tag{19}$$

Here in Eq. (19), P_2 represents the quadratic polynomial space, P_1 the linear polynomial space, and $H^1(\Omega)$ the Sobolev space defined by

$$H^1(\Omega) := \left\{ f \in L^2(\Omega) \;\middle|\; \frac{\partial f}{\partial x_j} \in L^2(\Omega),\ j = 1, \ldots, n \right\},$$

with the H^1-norm

$$\|f\|_{H^1(\Omega)} := \left(\|f\|_{L^2(\Omega)}^2 + \sum_{j=1}^{n} \left\| \frac{\partial f}{\partial x_j} \right\|_{L^2(\Omega)}^2 \right)^{1/2}.$$

To construct the weak formulation, let $\bar{W} = [H^1(\Omega)]^3$ be the test space for velocity and microrotation variables, and $Q = L^2(\Omega)$ be the pressure test space. Find $(U_h, V_h, W_h) \in \bar{W}_h$ and $P_h \in Q_h$ such that

$$\begin{aligned} &\frac{1}{\delta t} \int_{\Omega^{n+1}} U_h^{n+1} \tilde{U}_h \, d\Omega - \frac{1}{\delta t} \int_{\Omega^{n+1}} (U_h^n \circ X^n) \tilde{U}_h \, d\Omega - A_1 \int_{\Omega^{n+1}} \left\{ \left(U_h^n U_h^{n+1} \frac{\partial U_h^{n+1}}{\partial X^{n+1}} + U_h^{n+1} V_h^{n+1} \frac{\partial U_h^{n+1}}{\partial Y^{n+1}} \right) \frac{\partial \tilde{U}_h}{\partial X^{n+1}} \right. \\ &- \left(V_h^n V_h^{n+1} \frac{\partial V_h^{n+1}}{\partial Y^{n+1}} + U_h^{n+1} V_h^{n+1} \frac{\partial U_h^{n+1}}{\partial X^{n+1}} \right) \frac{\partial \tilde{U}_h}{\partial Y^{n+1}} - \left(2U_h^{n+1} \frac{\partial U_h^{n+1}}{\partial X^{n+1}} \frac{\partial U_h^{n+1}}{\partial X^{n+1}} + 2V_h^{n+1} \frac{\partial V_h^{n+1}}{\partial Y^{n+1}} \frac{\partial V_h^{n+1}}{\partial Y^{n+1}} \right. \\ &\left. \left. + U_h^{n+1} \frac{\partial V_h^{n+1}}{\partial X^{n+1}} \frac{\partial U_h^{n+1}}{\partial Y^{n+1}} + V_h^{n+1} \frac{\partial U_h^{n+1}}{\partial X^{n+1}} \frac{\partial U_h^{n+1}}{\partial Y^{n+1}} + U_h^{n+1} \frac{\partial V_h^{n+1}}{\partial Y^{n+1}} \frac{\partial U_h^{n+1}}{\partial X^{n+1}} + V_h^{n+1} \frac{\partial U_h^{n+1}}{\partial Y^{n+1}} \frac{\partial U_h^{n+1}}{\partial X^{n+1}} \right) \tilde{U}_h \right\} d\Omega \\ &+ A_2 \left\{ \int_{\Omega^{n+1}} \frac{\partial U_h^{n+1}}{\partial X^{n+1}} \frac{\partial \tilde{U}_h}{\partial X^{n+1}} \, d\Omega - \oint_{\Gamma} \tilde{U}_h \left(n_x \frac{\partial U_h^{n+1}}{\partial X^{n+1}} \right) d\Gamma + \int_{\Omega^{n+1}} \frac{\partial U_h^{n+1}}{\partial Y^{n+1}} \frac{\partial \tilde{U}_h}{\partial Y^{n+1}} \, d\Omega - \oint_{\Gamma} \tilde{U}_h \left(n_y \frac{\partial U_h^{n+1}}{\partial Y^{n+1}} \right) d\Gamma \right\} \\ &+ A_3 \int_{\Omega^{n+1}} W_h^{n+1} \frac{\partial \tilde{U}_h}{\partial Y^{n+1}} \, d\Omega + q_h \int_{\Omega^{n+1}} U_h^{n+1} \frac{\partial \tilde{U}_h}{\partial X^{n+1}} \, d\Omega - P_h^{n+1} \int_{\Omega^{n+1}} \frac{\partial \tilde{U}_h}{\partial X^{n+1}} \, d\Omega = 0, \end{aligned} \tag{20}$$

$$\frac{1}{\delta t}\int\limits_{\Omega^{n+1}} V_h^{n+1}\tilde{V}_h\,d\Omega-\frac{1}{\delta t}\int\limits_{\Omega^{n+1}}(V_h^n\circ Y^n)\tilde{V}_h\,d\Omega-A_4\int\limits_{\Omega^{n+1}}\Bigg\{\left(U_h^nU_h^{n+1}\frac{\partial V_h^{n+1}}{\partial X^{n+1}}+U_h^{n+1}V_h^{n+1}\frac{\partial V_h^{n+1}}{\partial Y^{n+1}}\right)\frac{\partial\tilde{V}_h}{\partial X^{n+1}}$$

$$-\left(V_h^nV_h^{n+1}\frac{\partial V_h^{n+1}}{\partial Y^{n+1}}+U_h^{n+1}V_h^{n+1}\frac{\partial V_h^{n+1}}{\partial X^{n+1}}\right)\frac{\partial\tilde{V}_h}{\partial Y^{n+1}}-\left(2U_h^{n+1}\frac{\partial U_h^{n+1}}{\partial X^{n+1}}\frac{\partial V_h^{n+1}}{\partial X^{n+1}}+2V_h^{n+1}\frac{\partial V_h^{n+1}}{\partial Y^{n+1}}\frac{\partial V_h^{n+1}}{\partial Y^{n+1}}\right.$$

$$\left.+U_h^{n+1}\frac{\partial V_h^{n+1}}{\partial X^{n+1}}\frac{\partial V_h^{n+1}}{\partial Y^{n+1}}+V_h^{n+1}\frac{\partial U_h^{n+1}}{\partial X^{n+1}}\frac{\partial V_h^{n+1}}{\partial Y^{n+1}}+U_h^{n+1}\frac{\partial V_h^{n+1}}{\partial Y^{n+1}}\frac{\partial V_h^{n+1}}{\partial X^{n+1}}+V_h^{n+1}\frac{\partial U_h^{n+1}}{\partial Y^{n+1}}\frac{\partial V_h^{n+1}}{\partial X^{n+1}}\right)\tilde{V}_h\Bigg\}\,d\Omega$$

$$+A_5\Bigg\{\int\limits_{\Omega^{n+1}}\frac{\partial V_h^{n+1}}{\partial X^{n+1}}\frac{\partial\tilde{V}_h}{\partial X^{n+1}}\,d\Omega-\oint\limits_{\Gamma}\tilde{V}_h\left(n_x\frac{\partial V_h^{n+1}}{\partial X^{n+1}}\right)d\Gamma+\int\limits_{\Omega^{n+1}}\frac{\partial V_h^{n+1}}{\partial Y^{n+1}}\frac{\partial\tilde{V}_h}{\partial Y^{n+1}}\,d\Omega-\oint\limits_{\Gamma}\tilde{V}_h\left(n_y\frac{\partial V_h^{n+1}}{\partial Y^{n+1}}\right)d\Gamma\Bigg\}$$

$$-A_6\int\limits_{\Omega^{n+1}}W_h^{n+1}\frac{\partial\tilde{V}_h}{\partial X^{n+1}}\,d\Omega+q_h\int\limits_{\Omega^{n+1}}V_h^{n+1}\frac{\partial\tilde{V}_h}{\partial Y^{n+1}}\,d\Omega-P_h^{n+1}\int\limits_{\Omega^{n+1}}\frac{\partial\tilde{V}_h}{\partial Y^{n+1}}\,d\Omega=0, \tag{21}$$

$$\frac{1}{\delta t}\int\limits_{\Omega^{n+1}}W_h^{n+1}\tilde{W}_h d\Omega-\frac{1}{\delta t}\left(W_h^n\ o\ X^n\right)\tilde{W}_h d\Omega-A_7\Bigg\{-\int\limits_{\Omega^{n+1}}\frac{\partial W_h^{n+1}}{\partial X^{n+1}}\frac{\partial\tilde{W}_h}{\partial X^{n+1}}d\Omega$$

$$+\oint\limits_{\Gamma}\tilde{W}_h\left(n_x\frac{\partial W_h^{n+1}}{\partial X^{n+1}}\right)d\Gamma-\int\limits_{\Omega^{n+1}}\frac{\partial W_h^{n+1}}{\partial Y^{n+1}}\frac{\partial\tilde{W}_h}{\partial Y^{n+1}}d\Omega+\oint\limits_{\Gamma}\tilde{W}_h\left(n_y\frac{\partial W_h^{n+1}}{\partial Y^{n+1}}\right)d\Gamma\Bigg\}$$

$$A_8\int\limits_{\Omega^{n+1}}\left(-V_h^{n+1}\frac{\partial\tilde{W}_h}{\partial X^{n+1}}+U_h^{n+1}\frac{\partial\tilde{W}_h}{\partial Y^{n+1}}-2W_h^{n+1}\tilde{W}_h\right)d\Omega=0, \tag{22}$$

for all $\tilde{U}_h, \tilde{V}_h, \tilde{W}_h \in \bar{W}_h$ and $P_h \in Q_h$. FEM approximation is achieved by using the approximate trial solution functions and trial test functions. These functions are the linear combination of nodal unknowns and shape functions which are linearly independent. Given below are the trial solution functions:

$$U_h=\sum_{j=1}^{m}U_j\xi_j,\quad V_h=\sum_{j=1}^{m}V_j\xi_j,\quad W_h=\sum_{j=1}^{m}W_j\xi_j,\quad P_h=\sum_{j=1}^{l}P_j\eta_j.$$

Similarly following trial approximated functions are defined for test spaces.

$$\tilde{U}_h, \tilde{V}_h, \tilde{W}_h=\sum_{i=1}^{m}(\tilde{U}_i, \tilde{V}_i, \tilde{W}_i)\xi_i,\quad q_h=\sum_{i=1}^{l}q_i\xi_i.$$

From Eqs. (20) to (22), we get the discretized system of nonlinear algebraic equations as

$$[K^*(U,V)]\{X^*\} = \{Q^*\}. \tag{23}$$

The matrix representation of Eq. (23) is written as

$$\underbrace{\begin{bmatrix} A_{11} & A_{12} & B_1 & A_{14} \\ A_{21} & A_{22} & B_2 & A_{24} \\ B_1^t & B_2^t & A_{33} & A_{34} \\ A_{41} & A_{42} & A_{43} & A_{44} \end{bmatrix}}_{K^*} \underbrace{\begin{bmatrix} U_h \\ V_h \\ P_h \\ W_h \end{bmatrix}}_{X^*} = \underbrace{\begin{bmatrix} Q_1 \\ Q_2 \\ Q_3 \\ Q_4 \end{bmatrix}}_{Q^*}. \tag{24}$$

Here, K^*, X^*, and Q^* are called block stiffness matrix, block solution and block boundary vectors, respectively. The local elemental entries of block stiffness matrix in Eq. (24) are given as

$$A_{11} = \frac{1}{\delta t}\int\limits_{\Omega^{n+1}} U_j^{n+1}\xi_j^{n+1}\xi_i^{n+1}d\Omega - \frac{1}{\delta t}\left(U_j^n\xi_j^n\ o\ X^n\right)\xi_i^{n+1}d\Omega + A_1\int\limits_{\Omega^{n+1}}\Bigg\{\Bigg(-U_j^n\xi_j^nU_j^{n+1}\xi_j^{n+1}$$

$$\frac{\partial\xi_j^{n+1}}{\partial X^{n+1}} - U_j^{n+1}\xi_j^{n+1}V_j^{n+1}\xi_j^{n+1}\frac{\partial\xi_j^{n+1}}{\partial Y^{n+1}}\Bigg)\frac{\partial\xi_i^{n+1}}{\partial X^{n+1}} + \Bigg(-U_j^{n+1}\xi_j^{n+1}V_j^{n+1}\xi_j^{n+1}\frac{\partial\xi_j^{n+1}}{\partial X^{n+1}}\Bigg)$$

$$\frac{\partial\xi_i^{n+1}}{\partial Y^{n+1}} + \Bigg(-2U_j^{n+1}\xi_j^{n+1}\frac{\partial\xi_j^{n+1}}{\partial X^{n+1}}\frac{\partial\xi_j^{n+1}}{\partial X^{n+1}} - U_j^{n+1}\xi_j^{n+1}\frac{\partial\xi_j^{n+1}}{\partial X^{n+1}}\frac{\partial\xi_j^{n+1}}{\partial Y^{n+1}} - U_j^{n+1}\xi_j^{n+1}\frac{\partial\xi_j^{n+1}}{\partial Y^{n+1}}$$

$$\frac{\partial\xi_j^{n+1}}{\partial X^{n+1}}\Bigg)\xi_i^{n+1}\Bigg\}d\Omega + \xi_i^{n+1}\int\limits_{\Omega^{n+1}}\xi_j^{n+1}\frac{\partial\xi_i^{n+1}}{\partial X^{n+1}}d\Omega - A_2\Bigg\{-\int\limits_{\Omega^{n+1}}\frac{\partial\xi_j^{n+1}}{\partial X^{n+1}}\frac{\partial\xi_i^{n+1}}{\partial X^{n+1}}d\Omega$$

$$-\int\limits_{\Omega^{n+1}}\frac{\partial\xi_j^{n+1}}{\partial Y^{n+1}}\frac{\partial\xi_i^{n+1}}{\partial Y^{n+1}}d\Omega\Bigg\},$$

$$A_{12} = A_1\int\limits_{\Omega^{n+1}}\Bigg\{\Bigg(-U_j^{n+1}\xi_j^{n+1}V_j^{n+1}\xi_j^{n+1}\frac{\partial\xi_j^{n+1}}{\partial Y^{n+1}}\Bigg)\frac{\partial\xi_i^{n+1}}{\partial X^{n+1}} + \Bigg(-V_j^n\xi_j^nV_j^{n+1}\xi_j^{n+1}\frac{\partial\xi_j^{n+1}}{\partial Y^{n+1}}$$

$$-U_j^{n+1}\xi_j^{n+1}V_j^{n+1}\xi_j^{n+1}\frac{\partial\xi_j^{n+1}}{\partial X^{n+1}}\Bigg)\frac{\partial\xi_i^{n+1}}{\partial Y^{n+1}} + \Bigg(-2V_j^{n+1}\xi_j^{n+1}\frac{\partial\xi_j^{n+1}}{\partial Y^{n+1}}\frac{\partial\xi_j^{n+1}}{\partial Y^{n+1}} - V_j^{n+1}\xi_j^{n+1}$$

$$\frac{\partial\xi_j^{n+1}}{\partial X^{n+1}}\frac{\partial\xi_j^{n+1}}{\partial Y^{n+1}} - V_j^{n+1}\xi_j^{n+1}\frac{\partial\xi_j^{n+1}}{\partial Y^{n+1}}\frac{\partial\xi_j^{n+1}}{\partial X^{n+1}}\Bigg)\xi_i^{n+1}\Bigg\}d\Omega,$$

$$A_{14} = A_3 \int\limits_{\Omega^{n+1}} W_j^{n+1} \xi_j^{n+1} \frac{\partial \xi_i^{n+1}}{\partial Y^{n+1}} d\Omega,$$

$$A_{21} = A_4 \int\limits_{\Omega^{n+1}} \Bigg\{ \Bigg(- U_j^n \xi_j^n U_j^{n+1} \xi_j^{n+1} \frac{\partial \xi_j^{n+1}}{\partial X^{n+1}} - U_j^{n+1} \xi_j^{n+1} V_j^{n+1} \xi_j^{n+1} \frac{\partial \xi_j^{n+1}}{\partial Y^{n+1}} \Bigg) \frac{\partial \xi_i^{n+1}}{\partial X^{n+1}}$$

$$+ \Bigg(- U_j^{n+1} \xi_j^{n+1} V_j^{n+1} \xi_j^{n+1} \frac{\partial \xi_j^{n+1}}{\partial X^{n+1}} \Bigg) \frac{\partial \xi_i^{n+1}}{\partial Y^{n+1}} + \Bigg(- 2U_j^{n+1} \xi_j^{n+1} \frac{\partial \xi_j^{n+1}}{\partial X^{n+1}} \frac{\partial \xi_j^{n+1}}{\partial X^{n+1}} - U_j^{n+1} \xi_j^{n+1}$$

$$\frac{\partial \xi_j^{n+1}}{\partial X^{n+1}} \frac{\partial \xi_j^{n+1}}{\partial Y^{n+1}} - U_j^{n+1} \xi_j^{n+1} \frac{\partial \xi_j^{n+1}}{\partial Y^{n+1}} \frac{\partial \xi_j^{n+1}}{\partial X^{n+1}} \Bigg) \xi_i^{n+1} \Bigg\} d\Omega,$$

$$A_{22} = \frac{1}{\delta t} \int\limits_{\Omega^{n+1}} V_j^{n+1} \xi_j^{n+1} \xi_i^{n+1} d\Omega - \frac{1}{\delta t} \Big(V_j^n \xi_j^n \; o \; Y^n \Big) \xi_i^{n+1} d\Omega + A_4 \int\limits_{\Omega^{n+1}} \Bigg\{ \Bigg(- U_j^{n+1} \xi_j^{n+1} V_j^{n+1}$$

$$\xi_j^{n+1} \frac{\partial \xi_j^{n+1}}{\partial Y^{n+1}} \Bigg) \frac{\partial \xi_i^{n+1}}{\partial X^{n+1}} + \Bigg(- V_j^n \xi_j^n V_j^{n+1} \xi_j^{n+1} \frac{\partial \xi_j^{n+1}}{\partial Y^{n+1}} - U_j^{n+1} \xi_j^{n+1} V_j^{n+1} \xi_j^{n+1} \frac{\partial \xi_j^{n+1}}{\partial X^{n+1}} \Bigg)$$

$$\frac{\partial \xi_i^{n+1}}{\partial Y^{n+1}} + \Bigg(- 2V_j^{n+1} \xi_j^{n+1} \frac{\partial \xi_j^{n+1}}{\partial Y^{n+1}} \frac{\partial \xi_j^{n+1}}{\partial Y^{n+1}} - V_j^{n+1} \xi_j^{n+1} \frac{\partial \xi_j^{n+1}}{\partial X^{n+1}} \frac{\partial \xi_j^{n+1}}{\partial Y^{n+1}} - V_j^{n+1} \xi_j^{n+1} \frac{\partial \xi_j^{n+1}}{\partial Y^{n+1}}$$

$$\frac{\partial \xi_j^{n+1}}{\partial X^{n+1}} \Bigg) \xi_i^{n+1} \Bigg\} d\Omega + \xi_i^{n+1} \int\limits_{\Omega^{n+1}} \xi_j^{n+1} \frac{\partial \xi_i^{n+1}}{\partial Y^{n+1}} d\Omega - A_5 \Bigg\{ - \int\limits_{\Omega^{n+1}} \frac{\partial \xi_j^{n+1}}{\partial X^{n+1}} \frac{\partial \xi_i^{n+1}}{\partial X^{n+1}} d\Omega$$

$$- \int\limits_{\Omega^{n+1}} \frac{\partial \xi_j^{n+1}}{\partial Y^{n+1}} \frac{\partial \xi_i^{n+1}}{\partial Y^{n+1}} d\Omega \Bigg\},$$

$$A_{24} = A_6 \int\limits_{\Omega^{n+1}} W_j^{n+1} \xi_j^{n+1} \frac{\partial \xi_i^{n+1}}{\partial X^{n+1}} d\Omega,$$

$$A_{44} = \frac{1}{\delta t} \int\limits_{\Omega^{n+1}} W_j^{n+1} \xi_j^{n+1} \xi_i^{n+1} d\Omega - \frac{1}{\delta t} \Big(W_j^n \xi_j^n \; o \; X^n \Big) \xi_i^{n+1} d\Omega - A_7 \Bigg\{ - \int\limits_{\Omega^{n+1}} \frac{\partial \xi_j^{n+1}}{\partial X^{n+1}} \frac{\partial \xi_i^{n+1}}{\partial X^{n+1}} d\Omega$$

$$- \int\limits_{\Omega^{n+1}} \frac{\partial \xi_j^{n+1}}{\partial Y^{n+1}} \frac{\partial \xi_i^{n+1}}{\partial Y^{n+1}} d\Omega \Bigg\} - A_8 \int\limits_{\Omega^{n+1}} \Big(- 2\xi_j^{n+1} \xi_i^{n+1} \Big) d\Omega,$$

$$A_{33}=0,\quad A_{34}=0,\quad A_{41}=\xi_j^{n+1}\frac{\partial\xi_i^{n+1}}{\partial Y^{n+1}},\quad A_{42}=-\xi_j^{n+1}\frac{\partial\xi_i^{n+1}}{\partial X^{n+1}},\quad A_{43}=0.$$

The entries A_{13}, A_{23} and A_{31}, A_{32} are the pressure matrices with their respective transposes can be written as

$$B_1^{ij}=-\eta_j^{n+1}\int\limits_{\Omega^{n+1}}\frac{\partial\xi_i^{n+1}}{\partial X^{n+1}}d\Omega,\quad B_2^{ij}=-\eta_j^{n+1}\int\limits_{\Omega^{n+1}}\frac{\partial\xi_i^{n+1}}{\partial Y^{n+1}}d\Omega,$$

$$(B_1^{ij})^t=-\xi_i^{n+1}\int\limits_{\Omega^{n+1}}\frac{\partial\eta_j^{n+1}}{\partial X^{n+1}}d\Omega,\quad (B_2^{ij})^t=-\xi_i^{n+1}\int\limits_{\Omega^{n+1}}\frac{\partial\eta_j^{n+1}}{\partial Y^{n+1}}d\Omega,$$

$$Q_1=\oint\limits_{\Gamma}\xi_i^{n+1}\left(n_x\frac{\partial\xi_j^{n+1}}{\partial X^{n+1}}\right)d\Gamma+\oint\limits_{\Gamma}\xi_i^{n+1}\left(n_y\frac{\partial\xi_j^{n+1}}{\partial Y^{n+1}}\right)d\Gamma,$$

$$Q_2=\oint\limits_{\Gamma}\xi_i^{n+1}\left(n_x\frac{\partial\xi_j^{n+1}}{\partial X^{n+1}}\right)d\Gamma+\oint\limits_{\Gamma}\xi_i^{n+1}\left(n_y\frac{\partial\xi_j^{n+1}}{\partial Y^{n+1}}\right)d\Gamma,$$

$$Q_3=0,\quad Q_4=\oint\limits_{\Gamma}\xi_i^{n+1}\left(n_x\frac{\partial\xi_j^{n+1}}{\partial X^{n+1}}\right)d\Gamma+\oint\limits_{\Gamma}\xi_i^{n+1}\left(n_y\frac{\partial\xi_j^{n+1}}{\partial Y^{n+1}}\right)d\Gamma.$$

The discrete system of non-linear algebraic equations in matrix form can be written as

$$\begin{bmatrix}A_{11}&A_{12}&B_1&A_{14}\\A_{21}&A_{22}&B_2&A_{24}\\B_1^T&B_2^T&0&0\\A_{41}&A_{42}&0&A_{44}\end{bmatrix}\begin{bmatrix}U_h\\V_h\\P_h\\W_h\end{bmatrix}=\begin{bmatrix}Q_1\\Q_2\\0\\Q_4\end{bmatrix}. \tag{25}$$

Equation (25) is solved using the Galerkin FEM implemented in FreeFEM++. This approach provides accurate and stable solutions for the coupled velocity, microrotation, and stress fields while allowing flexible discretization of the cavity geometry and straightforward implementation of boundary conditions. The code is used to compute the solution for varying parameters on the computational domain. The algorithm implemented is described in the following sub-section.

2.6 *Numerical algorithm (FreeFEM++ implementation)*

Step 1: Define the computational domain as a square cavity using the border command in FreeFEM++.

Step 2: Discretize and triangulate the domain into finite elements using the buildmesh command. The mesh is generated via the Delaunay-Voronoi algorithm with refinement near the moving lid and corners.

Step 3: Create the finite element spaces:

- P_2 elements for velocity components (u, v),
- P_1 elements for pressure p,

- P_2 elements for microrotation w, by using the fespace command.

Step 4: Initialize simulation parameters.

• **Step 4.1:** Set physical parameters Re, Er, Rf, and K.

• **Step 4.2:** Initialize velocity (u, v), pressure p, and microrotation w with zero fields.

• **Step 4.3:** Assemble the global stiffness matrix $\mathbf{K}$ and load vectors $\mathbf{F}_u$, $\mathbf{F}_w$ from the weak formulation using the varf command.

• **Step 4.4:** Solve the coupled algebraic system using the UMFPACK direct solver.

• **Step 4.5:** Apply the relaxation factor Rf to update velocity and microrotation fields for improved stability:

$$\mathbf{U}^{k+1} = (1-R_f)\mathbf{U}^k + R_f\mathbf{U}^*, \quad \mathbf{W}^{k+1} = (1-R_f)\mathbf{W}^k + R_f\mathbf{W}^*.$$

• **Step 4.6:** Check convergence criterion:

$$\|\mathbf{U}^{k+1} - \mathbf{U}^k\| + \|\mathbf{W}^{k+1} - \mathbf{W}^k\| < \varepsilon.$$

If not satisfied, return to Step 4.3.

Step 5: Save the solution data (velocity, pressure, microrotation, drag force, and stream function) for post-processing and visualization.

3. Result and discussion

3.1 *Validation and grid independence*

To validate the numerical results, the minimum and maximum values of the stream function and velocity components are computed. The grid independence study was carried out to ensure that the numerical solution of the problem under consideration is not influenced by the mesh resolution. Four progressively refined unstructured triangular meshes, labeled $M1$ to $M4$, were used. The number of elements and characteristic flow quantities at $Re = 200$ and $R_f = 0.01$ are summarized in Table 1. From Table 1, it is observed that as the mesh is refined the minimum and maximum stream function values ($\Psi_{\min}$ and $\Psi_{\max}$) gradually converge, with the change between the two finest meshes ($M3$ and $M4$) being negligible (less than 0.03%). The minimum horizontal velocity ($u_{\min}$) and vertical velocities ($v_{\min}$, $v_{\max}$) also exhibit a smooth convergence trend, with relative differences between $M3$ and $M4$ below 0.1%. This clearly indicates that the solution becomes essentially mesh independent beyond the $M3$ level. Therefore, for the remainder of the simulations, the $M3$ mesh with 14,398 unstructured triangular elements was adopted, providing a balance between computational accuracy and efficiency. The convergence trend also confirms the robustness of the numerical scheme applied on unstructured triangular elements and ensures that the flow features are accurately captured without being affected by the mesh resolution.

Table 1. Grid independence study against some flow characteristic variables at $Re = 200$ and $R_f = 0.01$

Mesh level	Elements	$\Psi_{\min}$	$\Psi_{\max}$	$u_{\min}$	$v_{\min}$	$v_{\max}$
$M1$	1,632	−0.000263520	0.085488	−0.410789	−0.909263	0.620285
$M2$	6,584	−0.000241100	0.092900	−0.377500	−0.845000	0.672000
$M3$	14,398	−0.000244500	0.092950	−0.378700	−0.844015	0.672802
$M4$	25,612	−0.000245135	0.092821	−0.379307	−0.845826	0.673491

The physical mechanism behind these variations is that higher R_f reduces frictional resistance and enhances translational motion of fluid particles, which increases kinetic energy. Consequently, the flow becomes smoother and less fluctuating, while velocity magnitudes grow. The Tables 2, 3, and 4 compares the present numerical results with those of Khan et al. [34]. It can be seen that a strong agreement is observed in terms of stream function extrema, velocity extrema and velocities at different positions in the domain, thereby validating the accuracy of the present FEM formulation.

Moreover, Table 2 shows that as the relaxation factor R_f increases, both $\Psi_{\min}$ and $\Psi_{\max}$ rise slightly, while $u_{\min}$ becomes less negative. In contrast, $v_{\min}$ decreases further, attaining more negative values, whereas $v_{\max}$ exhibits a slight increase.

Table 2. Comparison of present results with Khan et al. [34] for various R_f at $Re = 200$

R_f	0.0	5.0×10^{-3}	1.0×10^{-2}	0.0	5.0×10^{-3}	1.0×10^{-2}
Parameter		Khan et al. [34]			Present study	
$\Psi_{\min}$	−2.30958e-04	−2.39755e-04	−2.48093e-04	−0.000228599	−0.000237125	−0.000245135
$\Psi_{\max}$	9.1456e-02	9.21415e-02	9.28754e-02	0.091412	0.0920927	0.092821
$u_{\min}$	−4.52796e-01	−4.26949e-01	−3.79307e-01	−0.452793	−0.426947	−0.379307
$v_{\min}$	-	−7.42482e-01	−8.45826e-01	−0.695244	−0.742481	−0.845826
$v_{\max}$	-	6.21795e-01	6.7349e-01	0.593753	0.621798	0.673491

Table 3. u-velocity component for varying values of the fluid relaxation factor R_f with fixed Reynolds number $Re = 200$

	0.0	5.0e-03	1.0e-02	0.0	5.0e-03	1.0e-02
R_f		Khan et al. [34]			Present	
$u(0, -0.4375)$	−0.0137483	−0.01343	−0.01307	−0.0138023	−0.0134855	−0.0131326
$u(0, -0.375)$	−0.030435	−0.0301	−0.02972	−0.030473	−0.0301441	−0.0297663
$u(0, -0.3125)$	−0.0526477	−0.05262	−0.05256	−0.0526012	−0.0525704	−0.0525019
$u(0, -0.25)$	−0.0814902	−0.08209	−0.0827	−0.0813211	−0.0819026	−0.0824863
$u(0, -0.1875)$	−0.116168	−0.11768	−0.11925	−0.115901	−0.117358	−0.118891
$u(0, -0.125)$	−0.152827	−0.15526	−0.15788	−0.152479	−0.154873	−0.157444
$u(0, -0.0625)$	−0.183365	−0.18637	−0.18965	−0.18304	−0.186006	−0.189248
$u(0, 0)$	−0.197098	−0.19985	−0.20293	−0.196879	−0.199608	−0.202667
$u(0, 0.0625)$	−0.183887	−0.18551	−0.18744	−0.183818	−0.185434	−0.187365
$u(0, 0.125)$	−0.140708	−0.14078	−0.1411	−0.140779	−0.140866	−0.141201
$u(0, 0.1875)$	−0.0739784	−0.07263	−0.07142	−0.0741538	−0.0728288	−0.071643
$u(0, 0.25)$	0.00552624	0.007896	0.010288	0.00527294	0.00761584	0.00997587
$u(0, 0.3125)$	0.0919126	0.094687	0.097687	0.0915941	0.0943351	0.0972965
$u(0, 0.375)$	0.208309	0.21068	0.213527	0.207985	0.210322	0.21313
$u(0, 0.4375)$	0.471098	0.472924	0.475312	0.470901	0.472707	0.475071

Table 4. v-velocity component for varying values of the fluid relaxation factor R_f with fixed Reynolds number $Re = 200$

	0.0	5.0e-03	1.0e-02	0.0	5.0e-03	1.0e-02
R_f	Khan et al. [34]			Present		
$v(-0.4375, 0.0625)$	−0.0028463	−0.00295	−0.00304	−0.00282089	−0.00291704	−0.00300874
$v(-0.375, 0.0625)$	0.00278488	0.002681	0.002603	0.00280836	0.0027071	0.00263342
$v(-0.3125, 0.0625)$	0.0223357	0.022341	0.022417	0.0223205	0.0223253	0.0224004
$v(-0.25, 0.0625)$	0.11937	0.120209	0.121301	0.119151	0.119968	0.121033
$v(-0.1875, 0.0625)$	0.240211	0.243157	0.246468	0.239771	0.242665	0.245913
$v(-0.125, 0.0625)$	0.245026	0.248092	0.251353	0.244635	0.247655	0.250862
$v(-0.0625, 0.0625)$	0.211699	0.214401	0.217148	0.211439	0.21411	0.216822
$v(0.0, 0.0625)$	0.159801	0.161952	0.164013	0.1597	0.16184	0.163889
$v(0.0625, 0.0625)$	0.0885403	0.08944	0.090932	0.0885837	0.0898926	0.0909865
$v(0.125, 0.0625)$	−0.0018371	−0.00158	−0.00163	−0.00169661	−0.00142305	−0.00145684
$v(0.1875, 0.0625)$	−0.107099	−0.10807	−0.10939	−0.106906	−0.107851	−0.109151
$v(0.25, 0.0625)$	−0.214806	−0.21728	−0.22007	−0.214573	−0.217018	−0.219782
$v(0.3125, 0.0625)$	−0.29301	−0.29694	−0.30103	−0.292732	−0.296631	−0.300682
$v(0.375, 0.0625)$	−0.288203	−0.29211	−0.29585	−0.287915	−0.291785	−0.295484
$v(0.4375, 0.0625)$	−0.168197	−0.16994	−0.17139	−0.168013	−0.169736	−0.17116

3.2 *Discussion of results*

Table 5 presents the u-velocity component $u(x, y)$ along the y-axis for different values of the fluid relaxation factor R_f, while the Reynolds number is maintained at $Re = 200$. The velocity values are evaluated at selected locations along the vertical axis of the cavity to capture how the flow responds to variations in R_f. The chosen relaxation factors, $R_f = 0.0$, 5.0×10^{-3}, and 1.0×10^{-2}, represent a range of time-dependent effects in the fluid, which are known (see for instance Khan et al. [34]) to influence the numerical stability and convergence of finite element simulations, particularly in regions with high velocity gradients. From the table, it is observed that at lower positions in the cavity, such as $y = -0.4375$ and $y = -0.375$, the u-velocity component exhibits noticeable variation with increasing R_f. Specifically, as R_f increases, the magnitude of the velocity slightly decreases at $y = -0.4375$ while showing a small increase at $y = -0.375$. This suggests that the relaxation factor has a localized effect on the flow, particularly near the bottom of the cavity where the velocity gradients are stronger. The changes indicate that the presence of time relaxation allows the fluid to adjust more gradually to imposed boundary conditions and internal shear stresses, thereby affecting the local velocity distribution. In contrast, at higher positions, such as $y = 0.4375$, the u-velocity values are nearly identical across all relaxation factors, indicating that the flow is largely stabilized in the upper region of the cavity. This behavior is consistent with the expectation that relaxation effects are more pronounced in regions of higher shear or near boundaries, while the core flow is less sensitive to variations in R_f.

Table 5. u-velocity distribution along the y-axis for different values of R_f at $Re = 200$

y	$R_f = 0.0$	$R_f = 5.0 \times 10^{-3}$	$R_f = 1.0 \times 10^{-2}$
−0.4375	$u(0, -0.4375)$	$u(0, -0.4375)$	$u(0, -0.4375)$
−0.375	$u(0, -0.375)$	$u(0, -0.375)$	$u(0, -0.375)$
0.4375	$u(0, 0.4375)$	$u(0, 0.4375)$	$u(0, 0.4375)$

Table 6. v-velocity component at different x-axis positions for various values of R_f at $Re = 200$

x	$R_f = 0.1$	$R_f = 0.2$	$R_f = 0.3$	$R_f = 0.4$
-10	-0.5	-0.4	-0.3	-0.2
-5	-0.3	-0.2	-0.1	0.0
0	0.0	0.1	0.2	0.3
5	0.2	0.3	0.4	0.5
10	0.4	0.5	0.6	0.7

Table 6 complements these observations by presenting the v-velocity component at several x-axis locations for the same range of relaxation factors. The data clearly demonstrate that the vertical velocity changes sign across the domain, with downward flow (negative v) in some regions and upward flow (positive v) in others. This behavior is indicative of the recirculating flow patterns typically found in lid-driven cavities, where the fluid near the moving lid is transported in one direction while fluid near the opposite wall moves in the reverse direction. Increasing R_f slightly shifts the vertical velocity profiles, showing a small delay in the response of the fluid to boundary motion. This is consistent with the expected role of time relaxation in modulating microstructural rotational effects and reducing sharp variations in velocity across the cavity. The combined analysis of u- and v-velocity components provides a comprehensive picture of how R_f affects the flow, highlighting its importance in both numerical stability and physical representation of the fluid's behavior. Figure 2 presents the stream function contours within the lid-driven cavity for two different Eringen numbers, $Er = 0.5$ (Figure 2a) and $Er = 5.5$ (Figure 2b). The stream function provides a clear visualization of the flow pattern, vortex location, and circulation strength, reflecting the combined effects of viscous, inertial, and microstructural interactions. At the lower Eringen number, $Er = 0.5$, the primary vortex occupies a relatively central position in the cavity and exhibits moderate circulation. The streamlines are smooth and confined, indicating that the microinertia effects and microrotational influences are minimal, resulting in a flow structure that is closer to a classical Newtonian behavior. The smoothness and moderate curvature of the streamlines also suggest that the flow is stable and fully developed at this condition. When Er is increased to 5.5, notable changes occur in the stream function distribution. The primary vortex strengthens and shifts slightly upward, with streamlines becoming more concentrated near the top of the cavity. This behavior indicates that higher Er values enhance the effective resistance of the fluid to changes in motion, stabilizing the vortex structure and increasing confinement of the flow. The contours also suggest that higher Er suppresses smaller flow disturbances, reflecting the stabilizing effect of microinertia on the macroscopic flow field.

Figure 3 illustrates the distribution of microrotation velocities within the lid-driven cavity for varying values of the micropolar coupling constant, $K = 0.05$, 2.0, 3.0, and 5.0. The microrotation field reflects the local rotational activity of the fluid microelements, providing insight into how microstructural effects influence the macroscopic flow. At a low micropolar constant, $K = 0.05$ (Figure 3a), the microrotation velocities are relatively weak, and the contours are smooth and concentrated near the primary vortex. This indicates minimal influence of microstructural rotation on the overall flow, with the fluid behavior approaching that of a Newtonian or weakly micropolar fluid. The vortical structures are broad, and rotational activity is subdued, reflecting that the microelements contribute little to the momentum transfer. As K increases to 2.0 (Figure 3b), the intensity of microrotation strengthens, and localized high-velocity regions appear near the vortex core and along the cavity walls. This demonstrates that stronger micropolar coupling enhances the rotational degrees of freedom of microelements, leading to more pronounced rotational motion. The microrotation contours also show elongation along the shear layers, indicating increased interaction between microstructure rotation and macroscopic flow. Further increases in K to 3.0 and 5.0 (Figures 3c-d) reveal more complex microrotation patterns, with higher magnitudes and expanded regions of rotational activity. The vortices become more confined, and microrotation effects propagate deeper into the cavity interior. The trend indicates that stronger micropolarity reduces effective viscous resistance in shear layers while simultaneously amplifying local rotational motion, which can contribute to a reduction in drag, as observed in complementary drag force analyses.

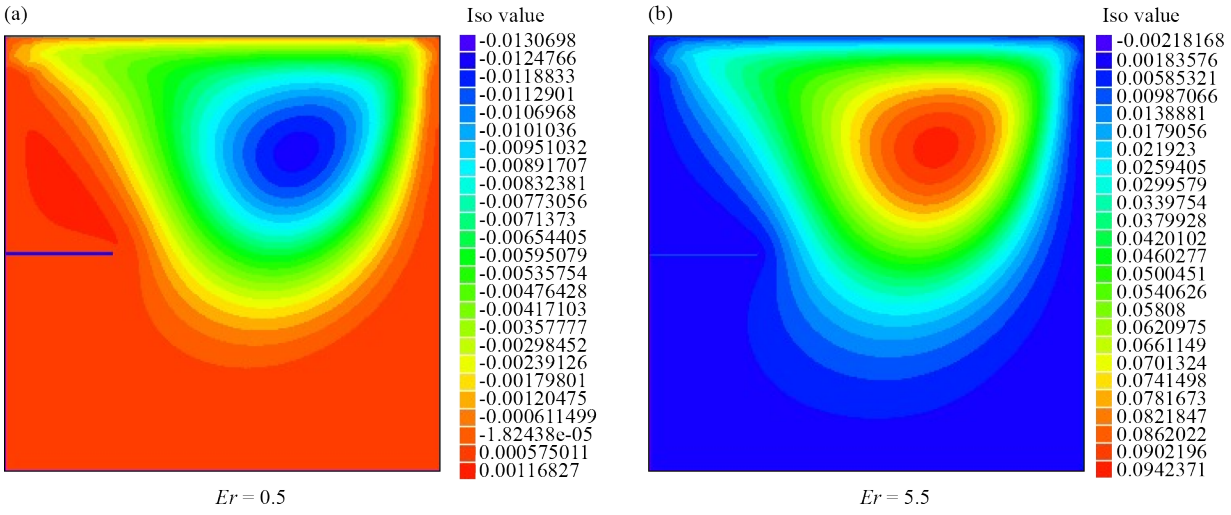


Figure 2. Stream function contours in the cavity for different values of the Eringen number (Er)

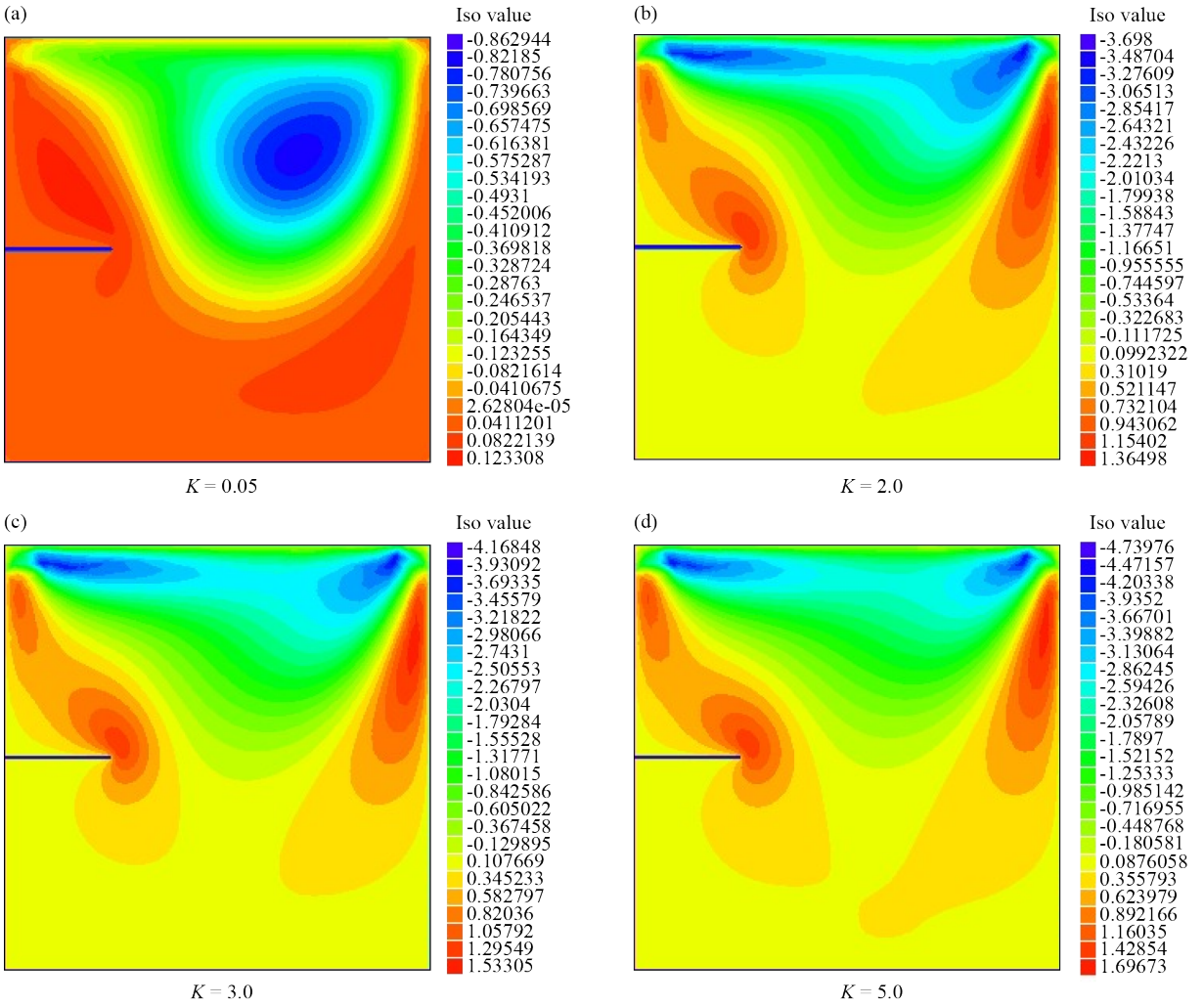


Figure 3. Distribution of microrotation velocities within the cavity for different values of the micropolar constant

Figure 4 illustrates the variation of the bottom wall drag force, Fd_{bottom}, with dimensionless time for different values of the Eringen number, $Er = 0.5$, 05×10^{-2}, 5×10^{-3}, and 5×10^{-5}. The Eringen number represents the ratio of microstructural effects to viscous effects, characterizing the influence of micropolarity in the fluid. At higher $Er = 0.5$, Fd_{bottom} exhibits a rapid decay to negative values, indicating that strong microstructural effects enhance rotational activity, opposing the macroscopic flow near the bottom wall. As Er decreases to 5×10^{-2} and 5×10^{-3}, the magnitude of the drag force reduces significantly, and the decay becomes smoother, reflecting weaker microstructural interactions. For very low $Er = 5 \times 10^{-5}$, the drag force remains nearly constant and slightly positive, suggesting that the fluid behavior approaches that of a Newtonian fluid with negligible micropolar effects. Overall, decreasing the Eringen number diminishes the rotational contribution of microelements to the drag, stabilizing the flow at the bottom wall.

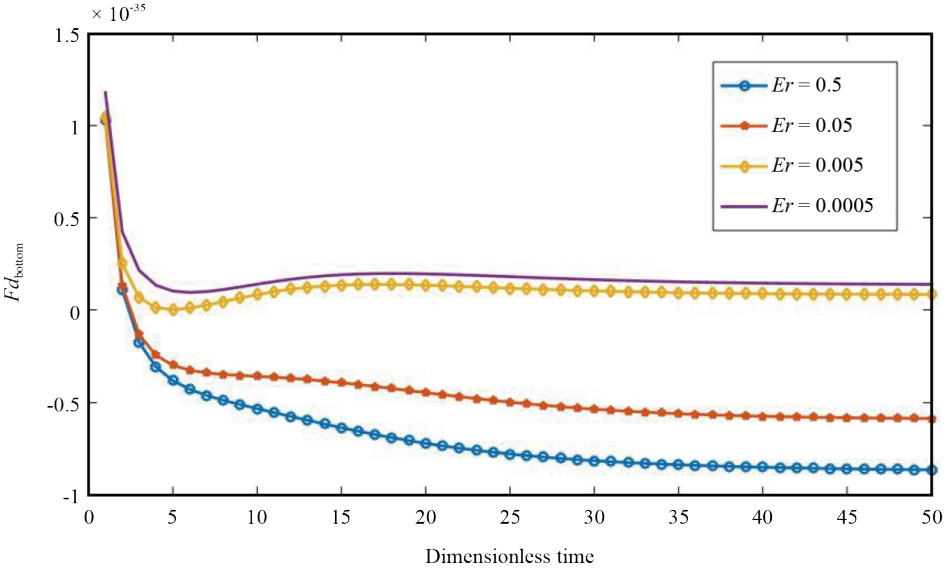


Figure 4. Variation of the bottom wall drag force (F_d) with horizontal position for different values of the Eringen number (Er), illustrating the effect of micropolarity on the wall drag

Figure 5 presents the velocity stream contours within the cavity for two values of the relaxation parameter, $R_f = 0.0$ and $R_f = 0.01$. The relaxation parameter R_f characterizes the rate at which microstructural rotational stresses relax, influencing microelement interactions in the micropolar fluid. At $R_f = 0.0$ (Figure 5a), the streamlines exhibit a symmetric, compact vortex structure concentrated near the cavity center, indicating minimal relaxation and sustained microstructural stresses that enhance local rotational activity. Introducing a small relaxation, $R_f = 0.01$ (Figure 5b), slightly modifies the vortex shape: the high-velocity region at the vortex core expands, and the contours become more diffused near the walls. This indicates that increased relaxation allows microelement rotations to adjust more rapidly to the surrounding flow, reducing local rotational stress and slightly increasing the overall flow momentum. The comparison highlights that even small relaxation effects can subtly modify the flow structure by balancing microstructural rotation and viscous dissipation.

Figure 6 shows the evolution of the bottom wall drag force, Fd_{bottom}, over dimensionless time for different relaxation parameters, $R_f = 0.0$, 0.01, and 0.02. At $R_f = 0.0$, the drag force initially peaks and then rapidly decays to a steady low value, reflecting the sustained microstructural stresses with no relaxation. Introducing a small relaxation $R_f = 0.01$ slightly increases the steady-state drag, indicating that partial stress relaxation reduces opposing microelement rotation, allowing more effective momentum transfer to the bottom wall. Further increase to $R_f = 0.02$ continues this trend, with the drag force reaching slightly higher steady values while maintaining the same overall decay profile. This demonstrates that increasing the relaxation parameter diminishes microstructural resistance near the wall, stabilizing the drag and enhancing the macroscopic flow response. The results confirm that relaxation effects provide a mechanism to moderate the influence of micropolar stresses on the drag behavior.

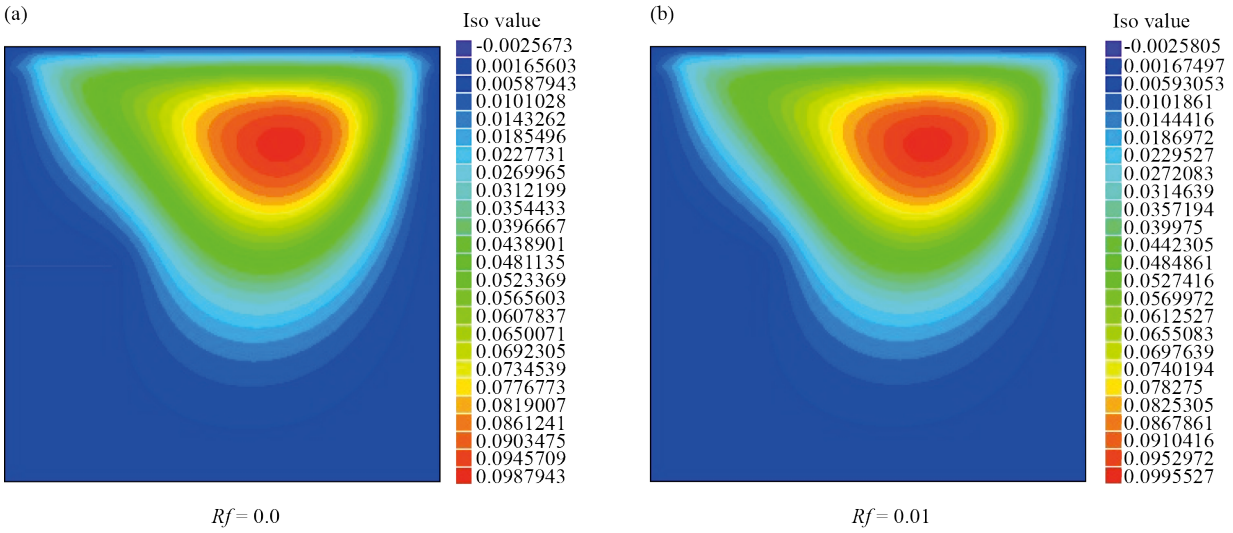


Figure 5. Velocity stream distribution within the cavity for different values of the relaxation time (Rf), illustrating the effect of microstructural relaxation on the flow field

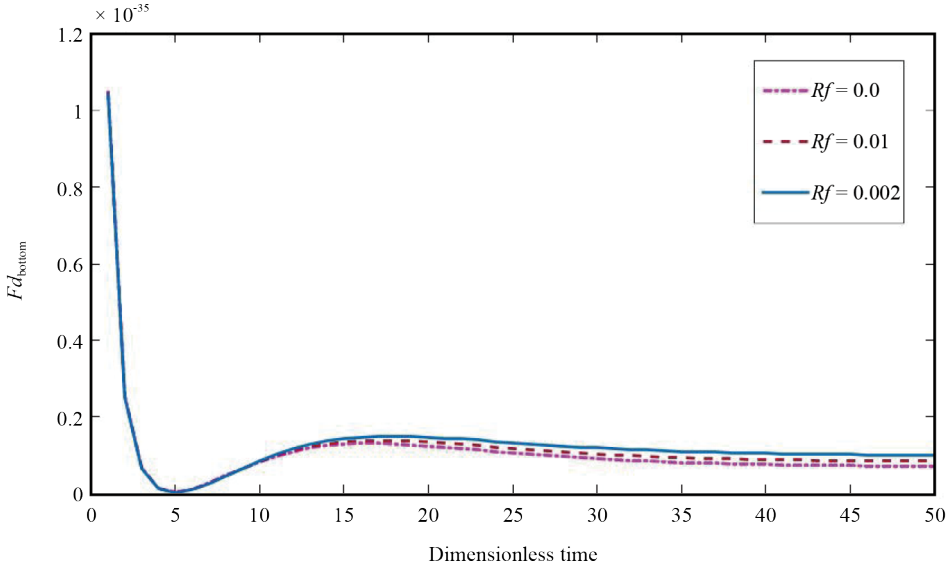


Figure 6. Variation of the bottom wall drag force (F_d) with horizontal position for different values of the relaxation time (Rf), showing the influence of microstructural relaxation on wall drag

Figure 7 shows the evolution of the bottom wall drag force, over dimensionless time for different values of the micropolar constant, $K = 0$, 1, and 2. The baseline case, $K = 0$, represents a classical Newtonian fluid where micro-rotational effects are absent. The drag force profile shows the resistance experienced by the bottom wall due to standard viscous shear. Introducing the micropolar effect with $K = 1$ causes a significant reduction in the steady-state drag force. This is because the micropolar fluid possesses an internal microstructure of elements that can rotate. This micro-rotation provides an additional degree of freedom for the fluid to respond to shear, acting as an internal lubricating mechanism. By absorbing shear energy into rotational motion, the microelements reduce the fluid's effective viscosity, thereby decreasing the momentum transferred to the stationary bottom wall. Further increasing the parameter to $K = 2$ amplifies this effect, leading to an even lower drag force. This demonstrates that strengthening the coupling between the micro-rotation and

the bulk fluid motion (a higher K) enhances the drag-reducing properties of the fluid. In summary, the results confirm that the micropolar constant K is a powerful parameter for controlling wall drag. By enabling micro-rotational degrees of freedom, it fundamentally alters the fluid's response to shear, reducing macroscopic resistance and lowering the force exerted on stationary surfaces.

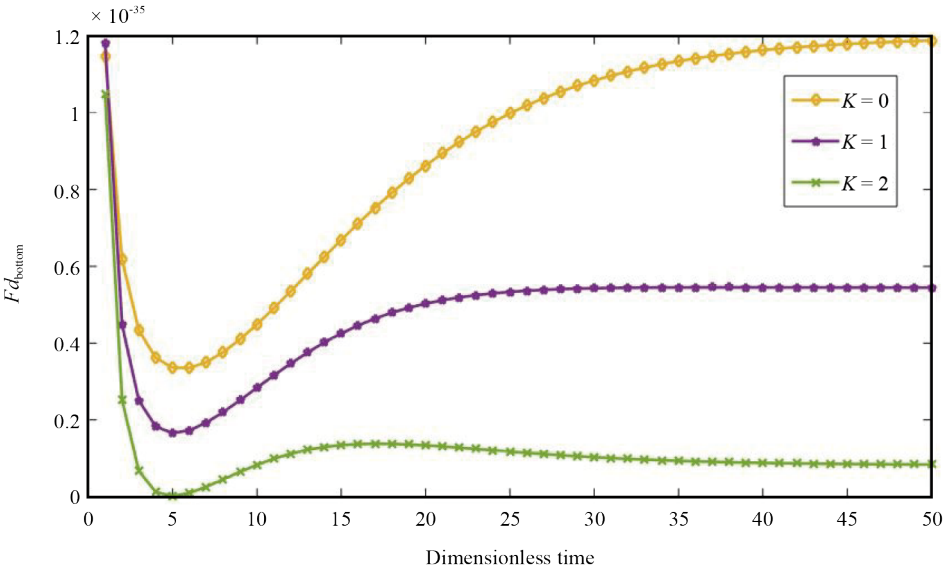


Figure 7. Variation of the bottom wall drag force (F_d) with horizontal position for different values of the micropolar coupling parameter (K), illustrating the effect of microstructural coupling on wall drag

Figure 8 illustrates the evolution of the drag force on the moving lid, over dimensionless time for different Eringen numbers, $Er = 0.005$, 0.05, and 0.5. At a low Eringen number, $Er = 0.005$, the microinertia of the fluid's substructure is minimal. The microelements can rotate relatively freely in response to the shear from the lid, contributing less to the overall resistance. Increasing the Eringen number to $Er = 0.05$ results in a noticeable increase in the magnitude of the drag force. The Eringen number quantifies the influence of microinertia. A higher Er means the microelements have more inertia and thus more strongly resist being set into rotation by the flow. This resistance to angular acceleration translates directly into a stronger coupling with the macroscopic flow, leading to increased viscous and inertial resistance felt by the lid. This trend is further confirmed at $Er = 0.5$, which shows the highest drag magnitude. At this level, the significant microinertia causes the fluid to behave as if it is "stiffer" or more resistant to shear. More of the momentum from the lid is required to overcome this internal rotational inertia, manifesting as a higher drag force. This demonstrates that the Eringen number directly governs drag by modulating the fluid's microinertial effects. Higher Er values suppress the free rotation of microelements, leading to enhanced momentum transfer from the moving lid to the fluid and consequently a greater drag force.

Figure 9 shows the evolution of the lid drag force, over time for varying micropolar constants, $K = 0$, 1, and 2. The Newtonian case ($K = 0$) exhibits a distinct oscillatory behavior before settling, which can be indicative of transient flow instabilities near the lid where shear is most intense. Introducing micropolar characteristics with $K = 1$ not only reduces the overall magnitude of the drag force but also significantly damps these initial oscillations, leading to a much smoother approach to the steady state. This dual effect occurs because the micro-rotations provide a new pathway for energy dissipation. Instead of contributing to flow instabilities, the shear energy is partially converted into the rotational energy of the microelements, which stabilizes the flow. Increasing the constant to $K = 2$ further reduces the drag and results in an even smoother, more stable transient profile. This highlights the role of K in both reducing steady-state resistance and enhancing the dynamic stability of the flow. In conclusion, this figure reveals that increasing the micropolar constant K

offers a dual benefit: it reduces the steady-state drag by lowering the effective viscosity and simultaneously enhances flow stability by providing an efficient mechanism for dissipating transient energy through micro-rotation.

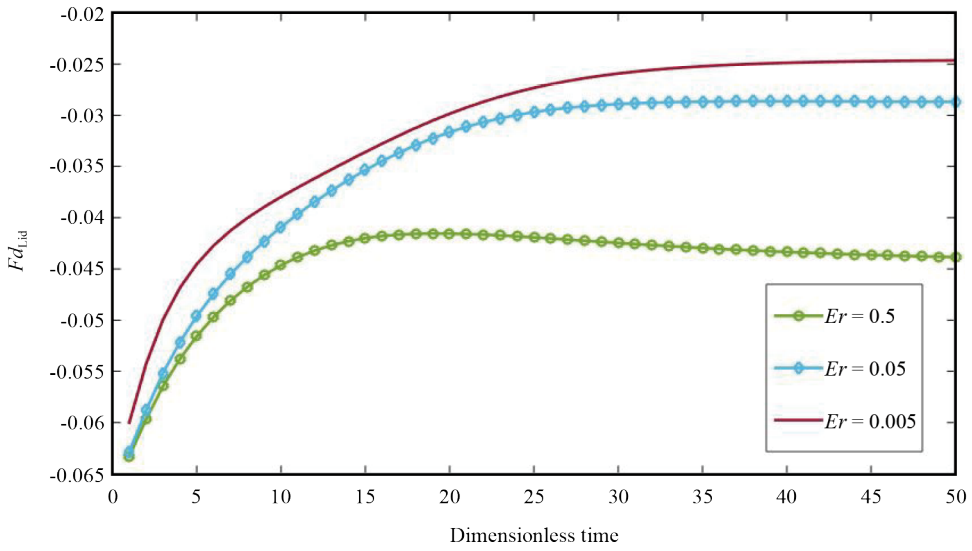


Figure 8. Variation of the top lid drag force (F_d) with horizontal position for different values of the Eringen number (Er)

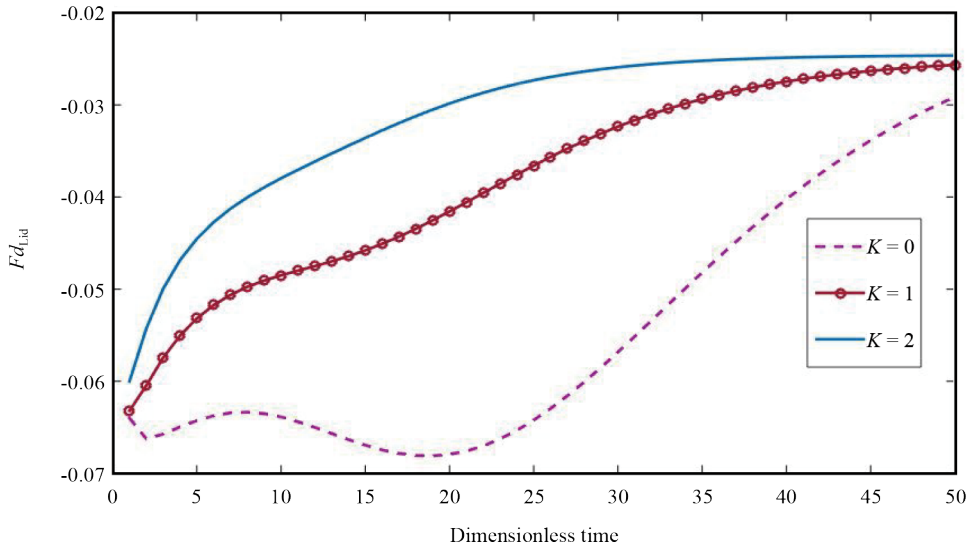


Figure 9. Variation of the top lid drag force (F_d) with horizontal position for different values of the micropolar coupling parameter (K), illustrating the effect of microstructural coupling on the lid wall drag

Figure 10 displays the impact of the fluid relaxation factor, $R_f = 0$, 0.01, and 0.02, on the drag force at the moving lid. At $R_f = 0$, the fluid has no viscoelastic memory; its response to stress is instantaneous. This curve serves as the baseline for a non-relaxing micropolar fluid. Introducing a small relaxation factor, $R_f = 0.01$, slightly increases the magnitude of the steady-state drag. This is because the relaxation factor introduces a time delay in the fluid's response, a key feature of viscoelasticity. This memory effect means that stress does not dissipate instantly, leading to the storage of elastic energy within the fluid structure. This stored elastic stress contributes to the overall resistance against the lid's motion. Further

increasing the relaxation time to $R_f = 0.02$ continues this trend, with the drag force reaching a slightly higher magnitude. A longer relaxation time enhances the fluid's elastic character, causing it to resist deformation more strongly due to its delayed response. This demonstrates that the relaxation parameter directly influences the viscoelastic contribution to drag. Increasing R_f enhances the fluid's elastic properties, leading to a delayed stress response and a corresponding increase in the macroscopic drag force experienced by the moving lid.

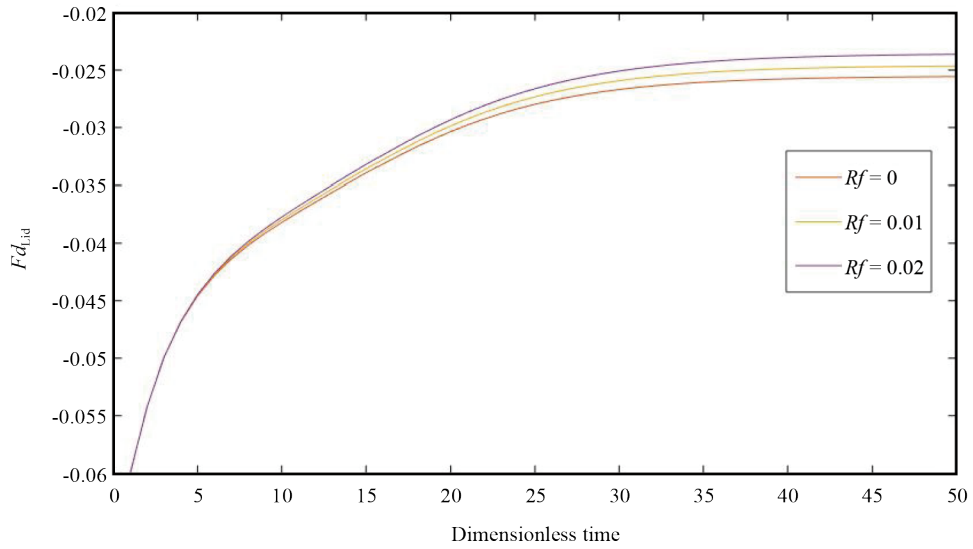
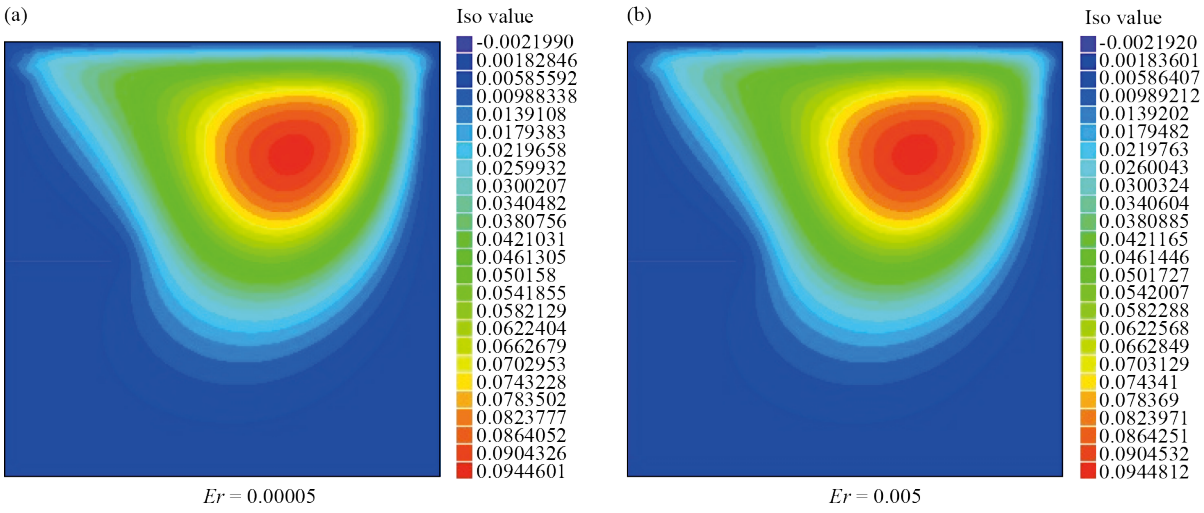


Figure 10. Variation of the top lid drag force (F_d) with horizontal position for different values of the relaxation time (Rf)

Figure 11 demonstrates the evolution of flow patterns for varying values of the Eringen number (Er). The Eringen number represents the ratio of micropolar viscous forces to traditional viscous forces. At lower values of Er (e.g., $Er = 0.00005$ and $Er = 0.005$), the streamlines display a distinct primary vortex structure centered within the cavity, characterized by strong circulation zones. As Er increases significantly to $Er = 5.5$, the flow structure undergoes a noticeable transformation. The primary vortex appears to shift and weaken in intensity, suggesting that higher micropolar viscous forces dampen the fluid motion. This indicates that as micropolar effects dominate, the resistance to flow increases, leading to a modification in the circulation patterns and a reduction in the overall convective strength within the cavity.



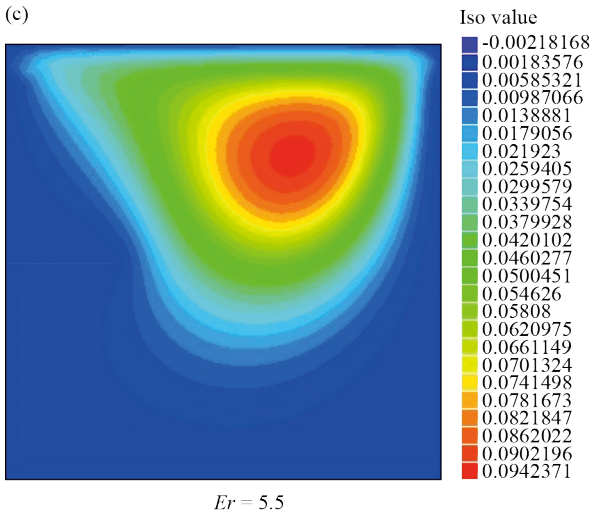


Figure 11. Stream function contours within the cavity for different values of the Eringen number (Er)

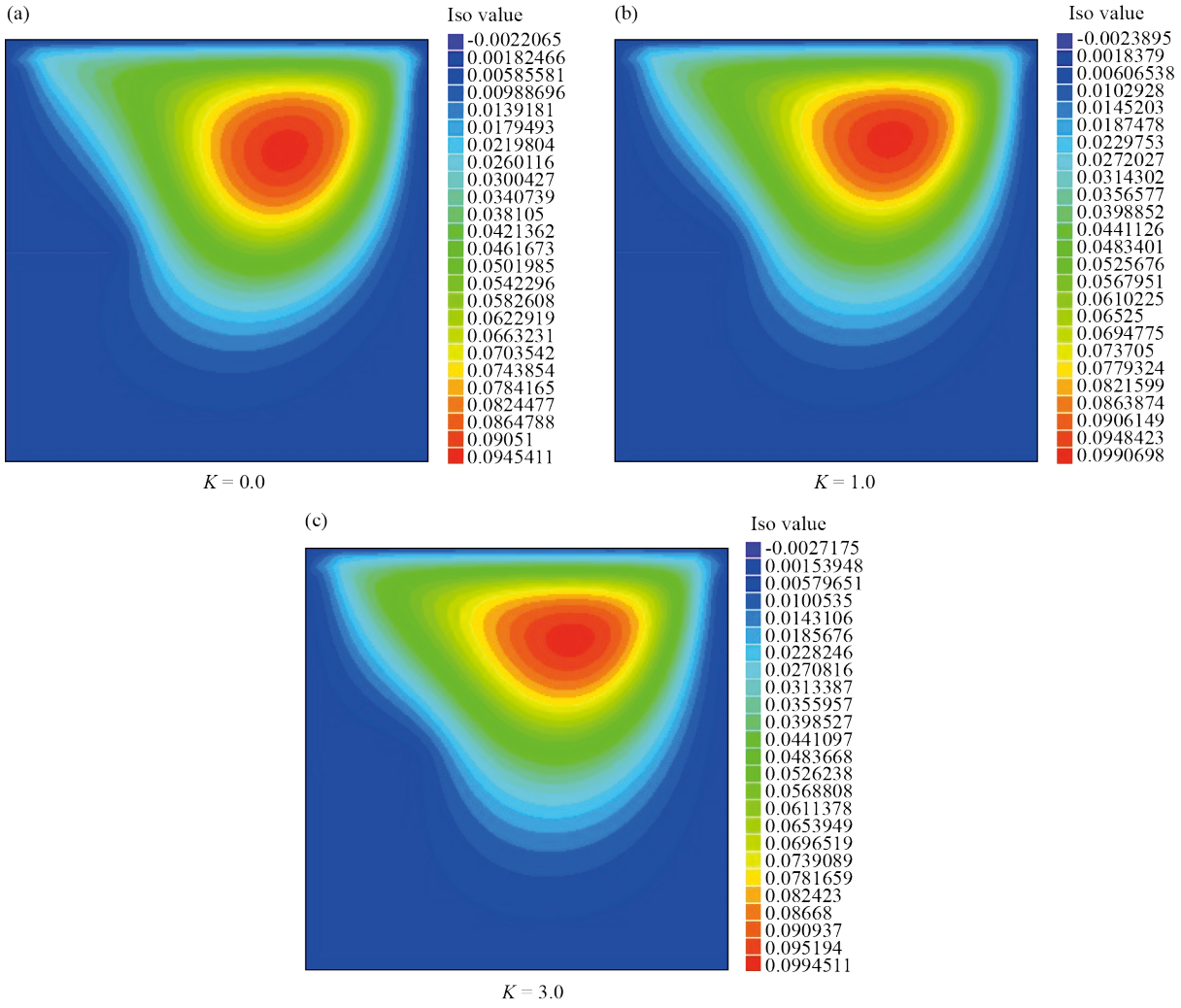


Figure 12. Stream function contours within the cavity for different values of the micropolar coupling parameter (K)

Figure 12 presents the stream contours for different values of the micropolar constant (K). The parameter K characterizes the coupling between the spin of the micro-elements and the macroscopic velocity field. At $K = 0.0$ (representing the Newtonian limit), the flow exhibits a classic vortex structure typical of lid-driven cavities. As K increases to 1.0 and subsequently to 3.0, the vortex core becomes more compressed and the flow topology is altered. The contour gradients suggest that increasing K leads to a suppression of the fluid velocity, as the rotational viscosity of the micro-elements extracts energy from the mean flow. Consequently, higher values of K result in a more stable, less intense flow circulation, highlighting the stabilizing effect of micropolar parameters on the fluid motion within the baffled enclosure.

Figure 13 shows the evolution of the total kinetic energy within the cavity over dimensionless time for different Eringen numbers, $Er = 0.005$, 0.05, and 0.5. For the lowest Eringen number, $Er = 0.005$, the system reaches a steady-state kinetic energy that reflects a balance where a significant portion of the input energy from the lid is dissipated through the relatively free rotation of the low-inertia microelements. As the Eringen number is increased to $Er = 0.05$, the steady-state kinetic energy of the system rises. This is because the higher microinertia makes it more difficult for the microelements to rotate. Consequently, less of the input energy is channeled into micro-rotational motion, and more is transferred into the bulk translational motion of the fluid. This effect is most pronounced at $Er = 0.5$, which exhibits the highest kinetic energy. The strong microinertial effects create a more rigid coupling between the microstructure and the macroscopic flow. This efficient momentum transfer from the lid results in a more vigorous and energetic circulation pattern throughout the cavity. The results confirm that the Eringen number is a key parameter in the energy distribution of the flow. By inhibiting energy dissipation through micro-rotation, a higher Er value channels more of the input power into the macroscopic kinetic energy of the fluid, leading to a more intense and ordered cavity flow.

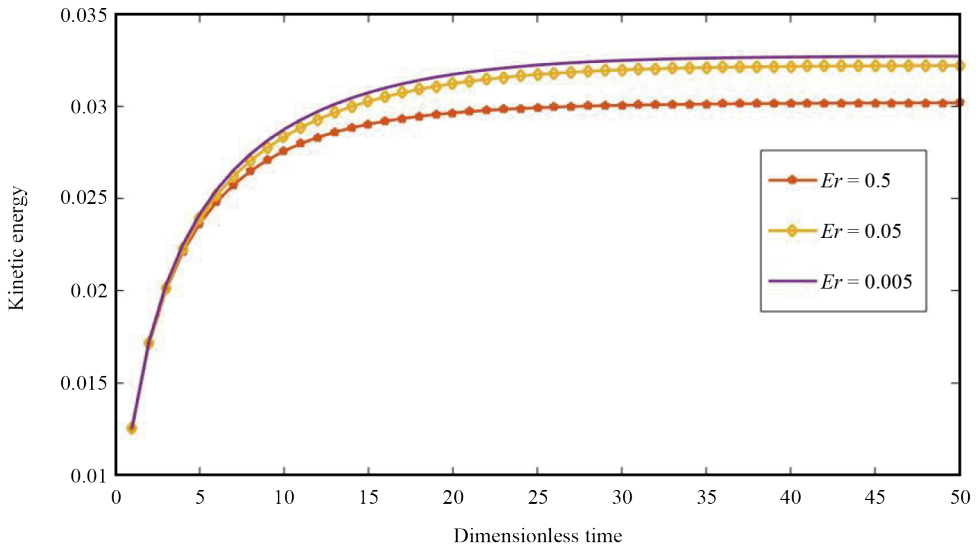


Figure 13. Variation of the total kinetic energy of the flow within the cavity for different values of the Eringen number (Er), illustrating the influence of micropolar effects on the flow intensity

Figure 14 illustrates the influence of the relaxation parameter on microrotation velocity within the cavity. It is observed that microrotation intensity increases as the relaxation factor becomes larger. Physically, the relaxation time represents the duration required for the fluid to adjust toward equilibrium after being subjected to deformation or external forcing. A larger relaxation time implies a delayed stress response, allowing the microstructural elements of the fluid additional time to undergo rotational motion. In the absence of relaxation effects, the fluid responds more abruptly to imposed shear, limiting the development of microrotation. As the relaxation factor increases, the response becomes more gradual, promoting stronger coupling between the translational flow and the rotational motion of microelements. This enhanced coupling leads to a noticeable amplification of microrotation velocities across the cavity domain. The

results indicate that relaxation time plays a significant role in regulating microstructural dynamics. Higher relaxation values support sustained rotational activity of fluid particles, thereby strengthening microrotation fields and modifying the overall flow behavior.

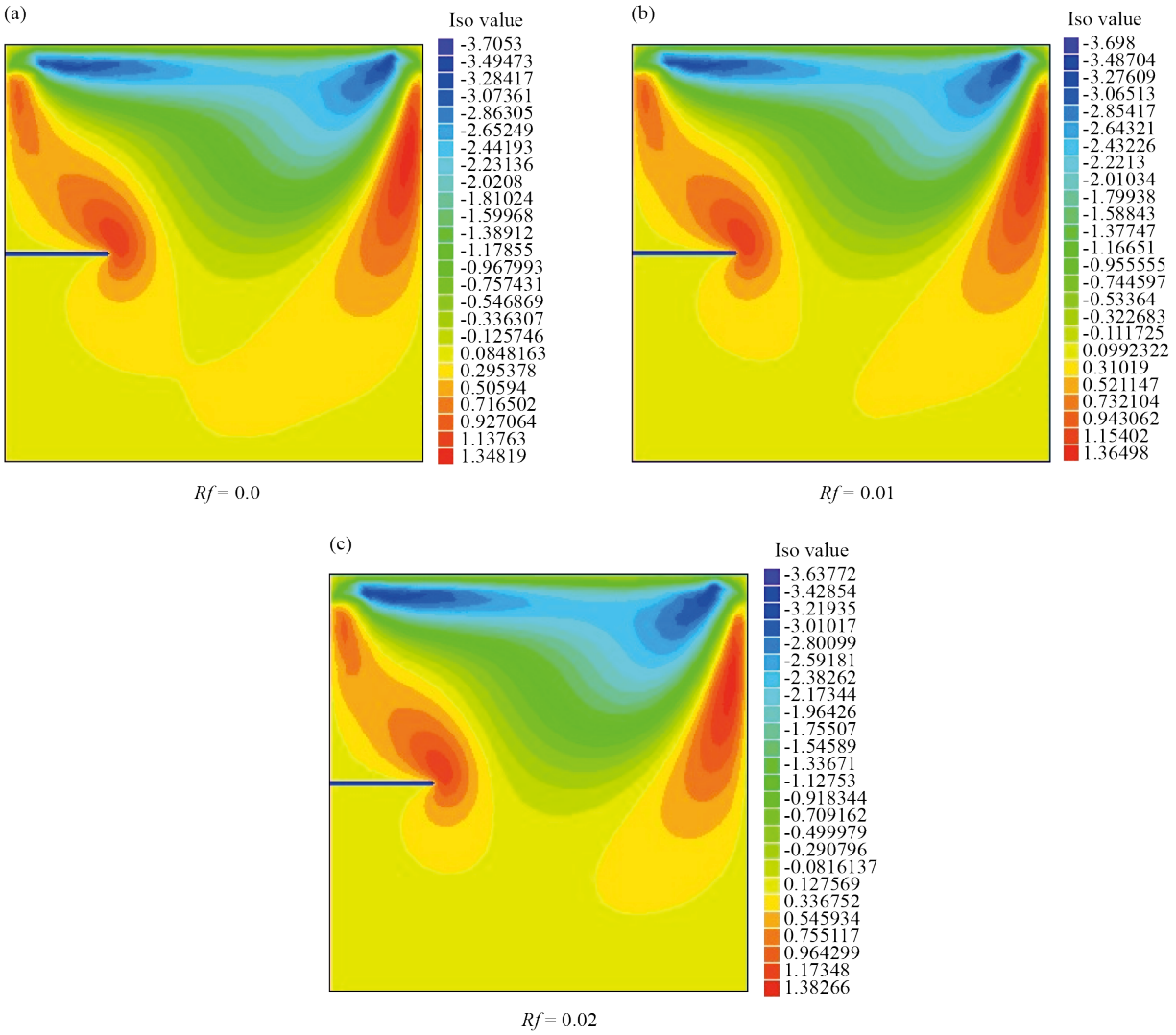


Figure 14. Distribution of the magnitude of microrotation velocities within the cavity for different values of the relaxation time (Rf), showing the enhancement of micro-rotations with increasing relaxation time

4. Conclusion

In this study, we conducted a detailed numerical investigation of micropolar fluid flow within a lid-driven cavity using the Finite Element Method (FEM) implemented in FreeFEM++. The work focused on analyzing the combined influence of the Eringen number (Er) and the fluid relaxation factor (Rf) on the drag force, stream function behavior, microrotation velocity, and kinetic energy. Through systematic simulations and careful validation against existing results in the literature [34], the following key conclusions can be drawn:

• The numerical solutions obtained from the present model demonstrated strong agreement with published results, confirming the accuracy and robustness of the variational formulation and FEM implementation. The introduction of a relaxation factor further improved numerical stability and convergence of the iterative scheme.

• Increasing Er significantly enhanced drag forces at both the cavity lid and bottom surfaces, reflecting stronger viscous and inertial resistance in the flow. Higher Er values also increased kinetic energy and produced more ordered and confined streamline structures. This confirms the Eringen number as a key control parameter in micropolar flow modeling, capturing the influence of microstructural rotation on macroscopic transport.

• The parameter Rf was found to directly regulate the stability and smoothness of cavity flow. Larger Rf values increased drag force due to delayed fluid response, but also enhanced microrotational activity by allowing more gradual adjustment of microelements to imposed shear. Relaxation effects therefore serve as an important mechanism for balancing convergence, stability, and physical realism in FEM-based micropolar flow simulations.

• Increasing the micropolar constant K reduced drag, owing to the intrinsic micro-rotational behavior of micropolar fluids, which lowers effective viscosity. At the same time, K amplified microrotation and stream function magnitudes, highlighting its role in strengthening microstructural effects while easing macroscopic resistance.

• The interplay between Er, Rf, and K revealed a delicate balance between viscous dissipation, inertial amplification, and microstructural dynamics. Eringen number governs the overall drag scaling, relaxation factor influences stability and microrotation magnitude, while the micropolar constant reduces resistance but intensifies rotational degrees of freedom. Together, these parameters provide a more complete physical picture of cavity flow beyond classical Newtonian assumptions.

The present study opens several promising directions for future research. Extending the analysis to three-dimensional cavities, considering heat transfer and Magnetohydrodynamic (MHD) effects, or incorporating more general non-Newtonian constitutive laws such as viscoelastic models could provide a richer understanding of micropolar flows in practical settings. Furthermore, coupling FEM simulations with experimental validation would be valuable to translate these theoretical insights into real-world applications. The current study is consistent with industry and innovation (Sustainable Development Goal 9) via the development of high-fidelity numerical modelling and control schemes relevant to the complex flow of micropolar and viscoelastic flows, which is required in the design and optimisation of new microfluidic and rheological systems. In addition, the proven ability to control the drag forces and increase the stability of flow can be regarded as a great contributor to the responsible consumption and production (sustainability development goal 12) since it enables the energy-efficient and resource-optimised flow of fluids. This research paper thus suggests several research avenues in the future. To the 3-D cavity arrangements of full three-dimensional analysis including heat-transfer, magnetohydrodynamic and solving as a more extensive set of non-Newtonian constitutive equations, would be more enlightening on the behaviour of micropolar flow under operating conditions of interest. Moreover, comparative validation of these theoretical results by finite-element simulations and experimental research would help to transfer these theoretical results into the most practical and industry-oriented applications.

Acknowledgment

This project is sponsored by Prince Sattam Bin Abdulaziz University (PSAU) as part of funding for its SDG Roadmap Research Funding Programme project number PSAU-2023-SDG-41.

Conflict of interest

The authors declare that they have no known competing financial or personal interests that could have appeared to influence the work reported in this paper.

References

[1] Zhang M, Yang E, Zeng J, Ji J, Tian F, Li L. Numerical study on oblique stretching of viscoelastic polymer film. *Journal of Non-Newtonian Fluid Mechanics*. 2021; 295: 104597. Available from: https://doi.org/10.1016/j.jnnfm.2021.104597.

[2] Czibula C, Seidlhofer T, Ganser C, Hirn U, Teichert C. Longitudinal and transverse low frequency viscoelastic characterization of wood pulp fibers at different relative humidity. *Materialia*. 2021; 16: 101094. Available from: https://doi.org/10.1016/j.mtla.2021.101094.

[3] Stieger S, Mitsoulis E, Walluch M, Ebner C, Kerschbaumer RC, Haselmann M, et al. On the influence of viscoelastic modeling in fluid flow simulations of gum acrylonitrile butadiene rubber. *Polymers*. 2021; 13(14): 2323. Available from: https://doi.org/10.3390/polym13142323.

[4] Sarow SA, Muna AK. Flows of viscous fluids in food processing industries: a review. *IOP Conference Series: Materials Science and Engineering*. 2020; 870(1): 012032. Available from: https://doi.org/10.1088/1757-899X/870/1/012032.

[5] Rubio-Hernández FJ. Rheological behavior of fresh cement pastes. *Fluids*. 2018; 3(4): 106. Available from: https://doi.org/10.3390/fluids3040106.

[6] Li G, Lauga E, Ardekani AM. Microswimming in viscoelastic fluids. *Journal of Non-Newtonian Fluid Mechanics*. 2021; 297: 104655. Available from: https://doi.org/10.1016/j.jnnfm.2021.104655.

[7] Qin B. *Flow behavior and instabilities in viscoelastic fluids: physical and biological systems*. PhD Thesis. University of Pennsylvania; 2018.

[8] Yuan C, Zhang HN, Li YK, Li XB, Wu J, Li FC. Nonlinear effects of viscoelastic fluid flows and applications in microfluidics: a review. *Proceedings of the Institution of Mechanical Engineers, Part C: Journal of Mechanical Engineering Science*. 2020; 234(22): 4390-4414.

[9] Zhu L, Lauga E, Brandt L. Self-propulsion in viscoelastic fluids: Pushers vs. pullers. *Physics of Fluids*. 2012; 24(5): 051902. Available from: https://doi.org/10.1063/1.4718446.

[10] Sebastian B, Dittrich PS. Microfluidics to mimic blood flow in health and disease. *Annual Review of Fluid Mechanics*. 2018; 50(1): 483-504. Available from: https://doi.org/10.1146/annurev-fluid-010816-060246.

[11] Haward SJ, Toda-Peters K, Shen AQ. Steady viscoelastic flow around high-aspect-ratio, low-blockage-ratio microfluidic cylinders. *Journal of Non-Newtonian Fluid Mechanics*. 2018; 254: 23-35. Available from: https://doi.org/10.1016/j.jnnfm.2018.02.009.

[12] Liu P, Liu H, Semenec L, Yuan D, Yan S, Cain AK, et al. Length-based separation of Bacillus subtilis bacterial populations by viscoelastic microfluidics. *Microsystems & Nanoengineering*. 2022; 8(1): 7. Available from: https://doi.org/10.1038/s41378-021-00333-3.

[13] Alves MA, Oliveira PJ, Pinho FT. Numerical methods for viscoelastic fluid flows. *Annual Review of Fluid Mechanics*. 2021; 53(1): 509-541. Available from: https://doi.org/10.1146/annurev-fluid-010719-060107.

[14] Mahapatra B, Bandopadhyay A. Electroosmosis of a viscoelastic fluid over non-uniformly charged surfaces: Effect of fluid relaxation and retardation time. *Physics of Fluids*. 2020; 32(3): 032005. Available from: https://doi.org/10.1063/5.0003457.

[15] Dey D. Viscoelastic fluid flow through an annulus with relaxation, retardation effects and external heat source/sink. *Alexandria Engineering Journal*. 2018; 57(2): 995-1001. Available from: https://doi.org/10.1016/j.aej.2017.01.039.

[16] Eldesoky IM, Abumandour RM, Abdelwahab ET. Analysis for various effects of relaxation time and wall properties on compressible Maxwellian peristaltic slip flow. *Zeitschrift für Naturforschung A*. 2019; 74(4): 317-331. Available from: https://doi.org/10.1515/zna-2018-0479.

[17] Cosserat EMP, Cosserat F. Théorie des corps déformables [Theory of deformable bodies]. *Nature*. 1909; 67: 81. Available from: https://doi.org/10.1038/081067a0.

[18] Eringen AC. Theory of micropolar fluids. *Journal of Mathematics and Mechanics*. 1966; 16(1): 1-18.

[19] Vladimir S. Flows of linear polymer solutions and other suspensions of rod-like particles: anisotropic micropolar-fluid theory approach. *Polymers*. 2021; 13(21): 3679. Available from: https://doi.org/10.3390/polym13213679.

[20] Sharma S, Lambha S, Mittal V, Verma R. Micropolar lubricant effects on the performance of partial journal bearings. *Proceedings of the Institution of Mechanical Engineers, Part J: Journal of Engineering Tribology*. 2023; 237(7): 1461-1470.

[21] Khan MS, Hackl K. Modeling of microstructures in a Cosserat continuum using relaxed energies. In: *Trends in Applications of Mathematics to Mechanics*. Springer; 2018. p.103-125. Available from: https://doi.org/10.1007/978-3-319-75940-1_6.

[22] Karvelas E, Sofiadis G, Papathanasiou T, Sarris I. Effect of micropolar fluid properties on the blood flow in a human carotid model. *Fluids*. 2020; 5(3): 125. Available from: https://doi.org/10.3390/fluids5030125.

[23] Eringen AC. *Microcontinuum Field Theories: I. Foundations and Solids*. Springer Science & Business Media; 2012. Available from: https://doi.org/10.1007/978-1-4612-0555-5.

[24] Saraswathy M, Prakash D, Durgaprasad P. MHD micropolar fluid in a porous channel provoked by viscous dissipation and non-linear thermal radiation: an analytical approach. *Mathematics*. 2022; 11(1): 183. Available from: https://doi.org/10.3390/math11010183.

[25] Almakki M, Mondal H, Sibanda P. Onset of unsteady MHD micropolar nanofluid flow with entropy generation. *International Journal of Ambient Energy*. 2022; 43(1): 4356-4369. Available from: https://doi.org/10.1080/01430750.2021.1890213.

[26] Yasmeen MM, Nabil TMED, Abou-Zeid MY, Mostapha DR, Oauf ME. Impacts of hall and ion slip currents with cattaneo-christov features on the peristaltic blood flow of sisko micropolar nanofluid inside an annulus through a porous medium. *Journal of Applied Nonlinear Dynamics*. 2024; 13(4): 735-760.

[27] Eldabe NT, Abouzeid M, Doaa R, Yasmeen M, Ouaf ME. Impacts of chemical reaction and electric field with Cattaneo-Christov theories on peristaltic transport of a hyperbolic micropolar nanofluid. *Egyptian Journal of Chemistry*. 2023; 66(7): 63-85.

[28] Yasmeen MM, El-Dabe NT, Abou-Zeid MY, Oauf ME, Mostapha DR. Peristaltic transport of carreau coupled stress nanofluid with cattaneochristov heat flux model inside a symmetric channel. *Journal of Advanced Research in Fluid Mechanics and Thermal Sciences*. 2022; 98(1): 1-17.

[29] Abd El-Aziz M, Afify AA. Influences of slip velocity and induced magnetic field on MHD stagnation-point flow and heat transfer of Casson fluid over a stretching sheet. *Mathematical Problems in Engineering*. 2018; 2018(1): 9402836.

[30] Narayana PS, Venkateswarlu B, Venkataramana S. Effects of Hall current and radiation absorption on MHD micropolar fluid in a rotating system. *Ain Shams Engineering Journal*. 2013; 4(4): 843-854. Available from: https://doi.org/10.1016/j.asej.2013.02.002.

[31] Goud BS. Heat generation/absorption influence on steady stretched permeable surface on MHD flow of a micropolar fluid through a porous medium in the presence of variable suction/injection. *International Journal of Thermofluids*. 2020; 7: 100044. Available from: https://doi.org/10.1016/j.ijft.2020.100044.

[32] Khan MS, Hameed I. A new magneto-micropolar boundary layer model for liquid flows-effect of micromagnetorotation (MMR). *arXiv:230808457*. 2023. Available from: https://doi.org/10.48550/arXiv.2308.08457.

[33] Hecht F. New development in FreeFem++. *Journal of Numerical Mathematics*. 2012; 20(3-4): 251-266. Available from: https://doi.org/10.1515/jnum-2012-0013.

[34] Khan MS, Memon MA, Bonyah E. Investigation of relaxation time on viscoelastic two-dimensional flow characteristics using FreeFem++. *Journal of Mathematics*. 2022; 2022(1): 4977793. Available from: https://doi.org/10.1155/2022/4977793.

[35] Hameed I, Khan MS. On the effects of micromagnetorotation in a micropolar cavity over two semi-circular rotating cylinders. *Multiscale and Multidisciplinary Modeling, Experiments and Design*. 2025; 8(10): 457. Available from: https://doi.org/10.1007/s41939-025-01053-1.